

Preconditioned Score-based Generative Models

Hengyuan Ma, Li Zhang, Xiatian Zhu, Jianfeng Feng

Abstract—Score-based generative models (SGMs) have recently emerged as a promising class of generative models. However, a fundamental limitation is that their sampling process is slow due to a need for many (*e.g.*, 2000) iterations of sequential computations. An intuitive acceleration method is to reduce the sampling iterations which however causes severe performance degradation. We assault this problem to the ill-conditioned issues of the Langevin dynamics and reverse diffusion in the sampling process. Under this insight, we propose a model-agnostic *preconditioned diffusion sampling* (PDS) method that leverages matrix preconditioning to alleviate the aforementioned problem. PDS alters the sampling process of a vanilla SGM at marginal extra computation cost, and without model retraining. Theoretically, we prove that PDS preserves the output distribution of the SGM, no risk of inducing systematical bias to the original sampling process. We further theoretically reveal a relation between the parameter of PDS and the sampling iterations, easing the parameter estimation under varying sampling iterations. Extensive experiments on various image datasets with a variety of resolutions and diversity validate that our PDS consistently accelerates off-the-shelf SGMs whilst maintaining the synthesis quality. In particular, PDS can accelerate by up to $29\times$ on more challenging high resolution (1024×1024) image generation. Compared with the latest generative models (*e.g.*, CLD-SGM, DDIM, and Analytic-DDIM), PDS can achieve the best sampling quality on CIFAR-10 at a FID score of 1.99. Our code is made publicly available to foster any further research <https://github.com/fudan-zvg/PDS>.



1 INTRODUCTION

As an alternative approach to generative adversarial networks (GANs) [1], recent score-based generative models (SGMs) [2], [3], [4], [5] have demonstrated excellent abilities in data synthesis (especially in high resolution images) with easier optimization [2], richer diversity [6], and more solid theoretic foundation [7]. Based on these progresses, SGMs and related models show great potential in various application [8] including high fidelity audio streams generation [9], [10], text-to-image generation [11], [12], [13], photo-realistic images editing [14], [15], [16], [17], video [18] generation, 3D shape generation [19], and scene graphs generation [8]. Starting from a sample initialized with a Gaussian distribution, a SGM produces a target sample by simulating a sampling process, typically a reverse diffusion, Langevin dynamics, or their combination (Alg. 1). Compared to the state-of-the-art GANs [20], [21], [22], a significant drawback with existing SGMs is *drastically slower generation* due to the need of taking many iterations for a sequential sampling process [4], [6], [11].

Formally, the discrete Langevin dynamic for sampling is typically formulated as

$$\mathbf{x}_t = \mathbf{x}_{t-1} + \frac{\epsilon_t^2}{2} \nabla_{\mathbf{x}} \log p_{\mathbf{x}^*}(\mathbf{x}_{t-1}) + \epsilon_t \mathbf{z}_t, 1 \leq t \leq T \quad (1)$$

where ϵ_t is the step size (a positive real scalar), \mathbf{z}_t is a standard Gaussian noise, and T is the iterations. Starting from a standard Gaussian sample \mathbf{x}_0 , with a total of T steps this sequential sampling process gradually transforms \mathbf{x}_0 to

the sample \mathbf{x}_T that obeys the target distribution $p_{\mathbf{x}^*}$, which is the steady-state distribution of the process. The discrete reverse diffusion for sampling is the reverse of a corrupting process starting from the data distribution $p_{\mathbf{x}^*}$

$$\mathbf{x}_t = \mathbf{x}_{t-1} + g_t \mathbf{z}_t, 1 \leq t \leq T, \quad (2)$$

where g_t is the step size. Typically, the discrete reverse diffusion is formulated as

$$\mathbf{x}_t = \mathbf{x}_{t-1} + \bar{g}_t^2 \nabla_{\mathbf{x}} \log \bar{p}_t(\mathbf{x}) + \bar{g}_t \mathbf{z}_t, 1 \leq t \leq T, \quad (3)$$

where $\bar{g}_t = g_{T-t}$, and $\bar{p}_t = p_{T-t}$ is the probabilistic distribution function of the state \mathbf{x}_{T-t} in the corrupting process at the time point t .

Since the evaluation of the gradient terms $\nabla_{\mathbf{x}} \log p_{\mathbf{x}^*}(\mathbf{x})$ (or $\nabla_{\mathbf{x}} \log \bar{p}_t(\mathbf{x})$) consumes the major time in the sampling process, for accelerating the sampling process, a straightforward way is to reduce the iterations T and proportionally expand the step size ϵ_t simultaneously, so that the number of calculating the gradient terms decreases, whilst keeping the total update magnitude. However, this often makes pretrained SGMs fail in image synthesis, as shown in Fig. 1.

Conceptually, the Langevin dynamics as defined in Eq. (1) can be considered as a special case of Metropolis adjusted Langevin algorithm (MALA) [23], [24], [25]. When the coordinates of the target dataset (*e.g.*, the pixel locations of a natural image) have a widely various scales or are strongly correlated, the sampling process will be *ill-conditioned*. As a result, the convergence of the sampling process is not guaranteed when the step sizes are large [25]. This explains the failure of sampling under a direct acceleration (Fig. 1). Observing that the reverse diffusion has a similar update rule as the Langevin dynamics (Eq. (1) vs. Eq. (3)), we conceive that it suffers the same ill-conditioned issue.

In light of this insight as above, we propose an efficient, model-agnostic *preconditioned diffusion sampling* (PDS) method for accelerating existing pretrained SGMs without the need for model retraining. The key idea is to make the

- Li Zhang and Hengyuan Ma contribute equally to this work. Li Zhang is the corresponding author with School of Data Science, Fudan University. E-mail: lizhangfd@fudan.edu.cn
- Hengyuan Ma and Jianfeng Feng are with Institute of Science and Technology for Brain-inspired Intelligence, Fudan University.
- Xiatian Zhu is with Surrey Institute for People-Centred Artificial Intelligence, CVSSP, University of Surrey.

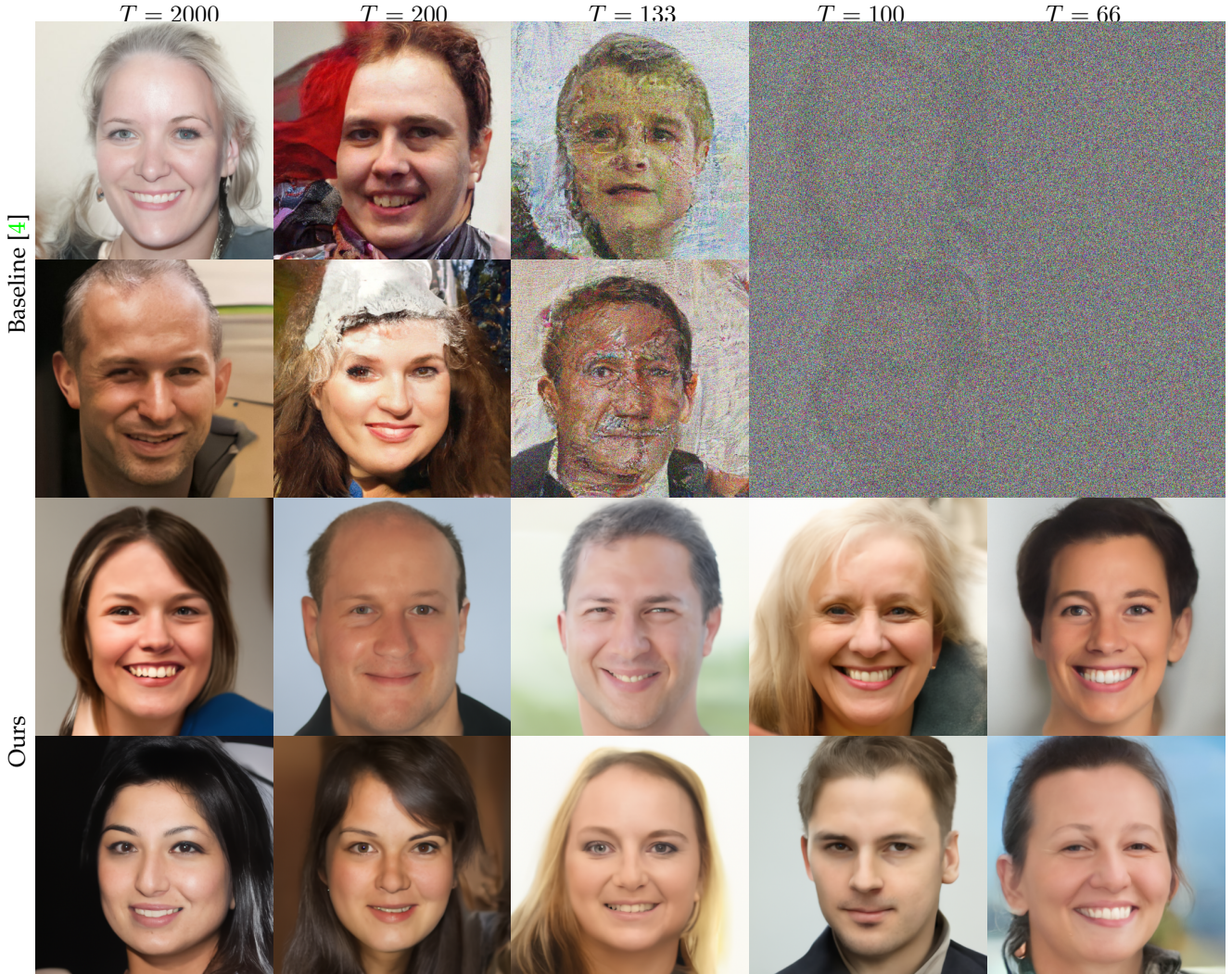


Fig. 1: Facial images at a resolution of 1024×1024 generated by NCSN++ [4] under a variety of sampling iterations (top) without and (bottom) with our PDS. It is evident that NCSN++ decodes quickly with increasingly reduced sampling iterations, which can be well solved with PDS. In terms of running speed for generating a batch of 8 images, PDS reduces the time cost of generating 8 human facial samples from 1920 sec (more than half an hours) to 68 sec (about one minute) on one NVIDIA RTX 3090 GPU. Dataset: FFHQ [21]. More samples in Appendix.

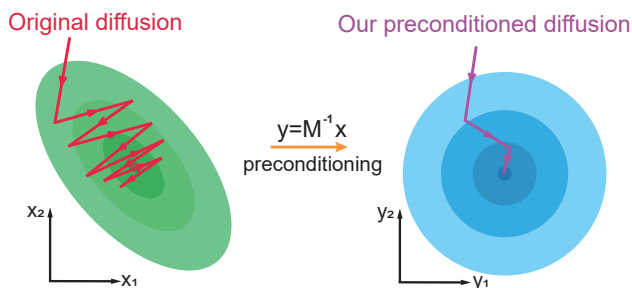


Fig. 2: Illustration of our preconditioning method for accelerating sampling process.

scales of the target distribution more similar along all the coordinates [23], [26] using a *matrix preconditioning* operation, hence solving the ill-conditioned problem of both the Langevin dynamics Eq. (1) and the reverse diffusion Eq. (3), as demonstrated in Fig. 2. Formally, we enrich the Langevin

dynamics Eq. (1) by reformulating the sampling process as

$$\mathbf{x}_t = \mathbf{x}_{t-1} + \frac{\epsilon_t^2}{2} \mathbf{M} \mathbf{M}^T \nabla_{\mathbf{x}} \log p_{\mathbf{x}^*}(\mathbf{x}_{t-1}) + \epsilon_t \mathbf{M} \mathbf{z}_t, \quad (4)$$

where \mathbf{M} is the newly introduced preconditioning matrix designed particularly for regulating the behavior of accelerated sampling processes. This proposed preconditioning matrix \mathbf{M} balances the scale of different coordinates of the sample space, hence alleviating the ill-conditioned issue. For the reverse diffusion Eq. (3), we also equip with a similar preconditioning

$$\mathbf{x}_t = \mathbf{x}_{t-1} + \bar{g}_t^2 \mathbf{M} \mathbf{M}^T \nabla_{\mathbf{x}} \log \bar{p}_t(\mathbf{x}_{t-1}) + \bar{g}_t \mathbf{M} \mathbf{z}_t, \quad (5)$$

Theoretically, we prove that PDS can preserve both the steady-state distribution of the original Langevin dynamics and the final-state distribution of the original reverse diffusion, with the assistance of Fokker-Planck equation [27] and related techniques. We construct the preconditioning operator \mathbf{M} using Fast Fourier Transform (FFT) [28], making its computational cost marginal.

In this work, we make the following **contributions**: **(1)** For sampling acceleration, we introduce a novel preconditioned diffusion sampling (PDS) process. PDS preconditions the existing sampling process for alleviating ill-conditioned issues, with theoretical guarantee of keeping the original target distributions in convergence. **(2)** With PDS, a variety of pretrained SGMs can be accelerated significantly for image synthesis at various spatial resolutions, without model retraining. In particular, PDS delivers $29\times$ reduction in wall-clock time for high-resolution (1024×1024) image synthesis. Compared with latest alternatives (*e.g.*, CLD-SGM [29], DDIM [30], and Analytic-DDIM [31]), PDS achieves superior performance on CIFAR-10 (FID score 1.99).

A preliminary version of this work was presented in ECCV 2022 [32]. In this paper, we have further extended our conference version as follows: **(i)** We reveal that the sampling process of the original SGMs is insensitive to the structural data (Sec. 3.4); **(ii)** We provide more theoretical explanation including its effect of preserving the final-state distribution of the reverse diffusion during sampling (Sec. 4.3); **(iii)** We conduct more quantitative experiments, including an extra dataset (CelebA), more iteration budgets evaluation, and comparing with more acceleration methods in both SGMs and DDPMs; **(iv)** We investigate the parameter space of PDS more comprehensively, resulting in further performance improvement; **(v)** We develop a theory easing the process of estimating proper parameter (Sec. 6.3) with experimental validation (Sec. 7.3).

2 RELATED WORK

Sohl-Dickstein *et al.* [33] first proposed to sequentially corrupt a target data distribution with Gaussian noises and train a model to learn the backward process to recover the target data distribution, inspired by non-equilibrium statistical physics. Exploring this procedure later on, Song and Ermon [2] proposed first SGMs, the noise conditional score network (NCSN). They [3] further proposed NCSNv2 for higher resolution image generation (*e.g.*, 256×256) by scaling noises and improving stability with moving average. Summarizing all the previous SGMs into a unified framework based on the stochastic differential equation (SDE), Song *et al.* [4] proposed NCSN++ to generate high-resolution images via numerical SDE solvers for the first time. Bortoli *et al.* [7] provided the first quantitative convergence results for SGMs. Vahdat *et al.* [34] trained SGMs in a latent space with the variational autoencoder framework. As another class of relevant generative models, denoising diffusion probabilistic models (DDPMs) [11], [35], [36], [37] also demonstrate excellent performance on image synthesis. They are mostly trained by maximizing an evidence lower bound (ELBO).

There are some recent works on improving the sampling quality of SGMs and DDPMs. Song *et al.* [30] proposed DDIMs by improving the sampling of DDPMs via a non-Markovian sampling process. Liu *et al.* [38] further improved DDIMs by implementing the sampling process near a manifold to guarantee that the model can fit the ground-truth score function well. Kingma *et al.* [39] proposed variational diffusion models to learn the noise schedule during training with another neural network for higher log-likelihood of the sampling results. Using the Hamiltonian

Monte Carlo methods [40], Dockhorn *et al.* [29] extended the sample space of SGMs with a velocity vector, and proposed critically-damped Langevin diffusion (CLD) based SGMs. Jolicœur-Martineau *et al.* [41] used a numerical SDE solver with adaptive step sizes to accelerate SGMs. A number of recent works [42], [43], [44] have utilized the concept of knowledge distillation to expedite the sampling process of DDPMs. Their common idea is a progressive distillation approach, involving the iterative refinement of a pretrained model. In comparison, our proposed PDS comes with a unique advantage of not requiring to train additional models for sampling acceleration.

As our PDS, some prior methods utilize non-isotropic noises to accelerate the sampling process. Jiang *et al.* [45] restricted the sampling process in a linear subspace where the data reside to accelerate the convergence of the sampling process. This might help with the illcondition issue and convergence speed, as the space of sampling decreases. However, our PDS directly adjusts the scales of different coordinates of the sampling space for alleviating ill-condition issue, without the need for subspace restriction. Nichol and Dhariwal [46] learned an additional variance vector during training a DDPM. Instead we exploit a preconditioning matrix simply estimated from the training data, without the need of training extra parameters. With diagonal covariance matrices, Bao *et al.* [31], [47] given the analytical formulation of a sequential of diagonal covariance matrices that maximizes the ELBO between the corrupting process and the sampling process for better sample performance. In comparison, our method is more efficient without solving a complex optimization problem.

However, these above methods are limited in the following aspects: **(1)** They tend to introduce much extra computation. For example, CLD-SGMs double the dimension of data due to learning the velocity of the diffusion. Jolicœur-Martineau *et al.* [41] added a high-order numerical solver that increases the number of calling the SGM, resulting in much more cost. With our PDS, the only extra calculation relates the preconditioning matrix that can be efficiently implemented by Fast Fourier Transform. As a result, PDS yields marginal extra computation to the vanilla SGMs. **(2)** They often improve a *single specific* SGM/DDPM while our PDS is able to accelerate three different SGMs (NCSN [2], NCSNv2 [3], and NCSN++ [4]). **(3)** Unlike our work, none of previous methods has demonstrated the scalability to more challenging high-resolution image generation tasks (*e.g.*, FFHQ facial images with 1024×1024 resolution).

3 PRELIMINARIES

3.1 Score matching

Assume that we observe i.i.d. samples from an unknown distribution $p_{\mathbf{x}^*}(\mathbf{x})$ of random vector $\mathbf{x} \in \mathbb{R}^d$, parameterized as $p_{\mathbf{x}^*}(\cdot; \theta)$ with θ the learnable parameters. In a non-normalized statistical learning setting, we have an explicit expression for $p_{\mathbf{x}^*}(\cdot; \theta)$ up to a normalization factor $Z(\theta)$

$$p_{\mathbf{x}^*}(\mathbf{x}; \theta) = \frac{1}{Z(\theta)} q(\mathbf{x}; \theta), \forall \mathbf{x} \in \mathbb{R}^d \quad (6)$$

where $Z(\theta) = \int_{\mathbf{x} \in \mathbb{R}^d} q(\mathbf{x}; \theta) d\mathbf{x}$ normalizes q so that it becomes a well-defined probabilistic distribution function. The

normalization factor $Z(\theta)$ is often intractable both analytically and numerically, especially for high-dimensional (d) data. This makes direct learning of $p_{\mathbf{x}^*}(\cdot; \theta)$ challenging.

Score matching is an effective approach to solving this challenge [48]. Specifically, a model $\mathbf{s}_\theta(\cdot)$ is trained to directly approximate the *score function* $\mathbf{s}_{\mathbf{x}^*}(\cdot) := \nabla_{\mathbf{x}} \log p_{\mathbf{x}^*}(\cdot)$ through the objective

$$\mathbb{E}_{\mathbf{x}^* \sim p_{\mathbf{x}^*}} [\|\mathbf{s}_\theta(\mathbf{x}) - \mathbf{s}_{\mathbf{x}^*}(\mathbf{x})\|^2]. \quad (7)$$

At the absence of $Z(\theta)$, training with this objective is more tractable. [48] further proves that under some mild conditions, if $p_{\mathbf{x}^*}(\cdot) = p_{\mathbf{x}^*}(\cdot; \theta^*)$, the ground-truth parameters θ^* can be achieved by minimizing Eq. (7) to zero.

However, Eq. (7) can not be evaluated in more general cases where an expression of the score function about θ is absent. To address this, [49] proposes an equivalent, simpler objective inspired by denoising autoencoders

$$\mathbb{E}_{\mathbf{x} \sim p_{\mathbf{x}^*}} [\|\mathbf{s}_\theta(\mathbf{x}_\sigma) - \nabla_{\mathbf{x}_\sigma} \log p_\sigma(\mathbf{x}_\sigma | \mathbf{x})\|^2], \quad (8)$$

where $p_\sigma(\mathbf{x}_\sigma | \mathbf{x}) = \mathcal{N}(\mathbf{x}_\sigma; \mathbf{x}, \sigma^2 I)$. Formally, given a noised data sample \mathbf{x}_σ , the model $\mathbf{s}_\theta(\cdot)$ is trained to extract the Gaussian noise vector added into the sample. This denoises the sample corrupted by the noise, *i.e.*, subtracting the noise vector gives the original sample. It is proved that minimizing the objective Eq. (8) allows the model to fit the ground-truth score function $\mathbf{s}_{\mathbf{x}^*}$ of the data distribution [49].

3.2 Sampling from the Langevin dynamics

SGMs generate samples from a target distribution through iteratively evaluating the target score function. The first SGM, noise conditional score network (NCSN) [2] \mathbf{s}_θ , is trained on a series of score matching tasks via

$$\sum_{t=1}^T \sigma_t^2 \mathbb{E}_{\mathbf{x} \sim p_{\mathbf{x}^*}} [\|\mathbf{s}_\theta(\mathbf{x}_{\sigma_t}, \sigma_t) - \nabla_{\mathbf{x}_{\sigma_t}} \log p_{\sigma_t}(\mathbf{x}_{\sigma_t} | \mathbf{x})\|^2], \quad (9)$$

with the standard deviations $\{\sigma_t\}_{t=1}^T$ satisfies $0 < \sigma_1 < \sigma_2 < \dots < \sigma_T$. At inference, a NCSN generates samples from $p_{\mathbf{x}^*}$ through the discretized Langevin dynamics

$$\mathbf{x}_t = \mathbf{x}_{t-1} + \frac{\epsilon_t^2}{2} \nabla_{\mathbf{x}_{t-1}} \log p_{\mathbf{x}^*}(\mathbf{x}_{t-1}) + \epsilon_t \mathbf{z}_t, 1 \leq t \leq T, \quad (10)$$

where the initialization $\mathbf{x}_0 \sim \mathcal{N}(\mathbf{0}, I)$, $\log p_{\mathbf{x}^*}(\mathbf{x}_{t-1})$ is approximated by $\mathbf{s}_\theta(\mathbf{x}_{t-1}, \sigma_t)$ at a proper level of σ_t , $\epsilon_t > 0$ the step size, and T the iterations. With this process, we transform a Gaussian sample \mathbf{x}_0 to \mathbf{x}_T in the target distribution $p_{\mathbf{x}^*}$. The Langevin dynamics Eq. (10) works in that as $T \rightarrow +\infty$, the distribution of \mathbf{x}_t converges to a *steady-state distribution*, exactly $p_{\mathbf{x}^*}$ [25]. Improvements can be made by refining noise scales, iterations and step size, and using the moving average technique [3].

3.3 Reverse diffusion

Given the discretized corrupting (*i.e.*, forward) process

$$\mathbf{x}_0 \sim p_{\mathbf{x}^*}, \mathbf{x}_t = \mathbf{x}_{t-1} + g_t \mathbf{z}_t, 1 \leq t \leq T, \quad (11)$$

where $g_t = \sqrt{\sigma_t^2 - \sigma_{t-1}^2}$, an alternative generation strategy is by simulating a corresponding discretized reverse process

$$\mathbf{x}_t = \mathbf{x}_{t-1} + \bar{g}_t^2 \nabla_{\mathbf{x}} \log \bar{p}_t(\mathbf{x}) + \bar{g}_t \mathbf{z}_t, 1 \leq t \leq T, \quad (12)$$

where the initial distribution $\mathbf{x}_0 \sim \mathcal{N}(\mathbf{0}, I)$, $\bar{g}_t = g_{T-t}$, $\bar{p}_t = p_{T-t}$ is the probabilistic distribution function of \mathbf{x}_{T-t} in the forward process. In this way, the final-steady state \mathbf{x}_T of reverse diffusion obeys $p_{\mathbf{x}^*}$ [50]. Eq. (11) and (12) both are the discretized version of the corresponding stochastic differential equation (SDE). Hence, a numerical solver of SDE can be used to implement the sampling process, as realized in NCSN++ [4]. Specifically, NCSN++ learns to fit the gradient term $\nabla_{\mathbf{x}} \log p_{T-t}(\mathbf{x})$ through minimizing

$$\mathbb{E}_t \lambda_t \mathbb{E}_{\mathbf{x}_0 \sim p_{\mathbf{x}^*}} [\|\mathbf{s}_\theta(\mathbf{x}(t), t) - \nabla_{\mathbf{x}_t} \log p_t(\mathbf{x}_t | \mathbf{x}_0)\|^2], \quad (13)$$

where t is uniformly drawn from $\{1, \dots, T\}$, and λ_t is the weight at t . During sampling, NCSN++ updates the state in two steps (Alg. 1): (1) predicting with the reverse diffusion (Eq. (12)), (2) correcting with the Langevin dynamics (Eq. (10)). This improves both accuracy and stability. The variance exploding (VE) variant is the best among all NCSN++ models [4].

Algorithm 1 The sampling process of VE NCSN++

Input: The sampling iterations T , the score model \mathbf{s}_θ ;
Initialization: Draw $\mathbf{x}_0 \sim \mathcal{N}(\mathbf{0}, I)$;
for $t = 1$ **to** T **do**
 Predicting (reverse diffusion):
 Drawing $\mathbf{z}_t \sim \mathcal{N}(\mathbf{0}, I)$
 $\mathbf{x}'_t \leftarrow \mathbf{x}_{t-1} + \bar{g}_t^2 \mathbf{s}_\theta(\mathbf{x}_{t-1}, \bar{g}_t) + \bar{g}_t \mathbf{z}_t$
 Correcting (Langevin dynamics):
 Drawing $\mathbf{z}_t \sim \mathcal{N}(\mathbf{0}, I)$
 $\mathbf{x}_t \leftarrow \mathbf{x}'_t + \frac{\epsilon_t^2}{2} \mathbf{s}_\theta(\mathbf{x}'_t, \epsilon_t) + \epsilon_t \mathbf{z}_t$
end for
Output: \mathbf{x}_T

3.4 Limitation analysis

While having superior generating capability over GANs [1], SGMs run much slower. A direct way for acceleration is to reduce the iterations T and increase the step size ϵ_t proportionally (*i.e.*, one step for multiple ones). This however leads to severe degradation (see Fig. 1). This is partly because the sampling process is fundamentally limited in sampling structural data (*e.g.*, images), as elaborated below.

Theorem 1. Suppose $U \in \mathbb{R}^{d \times d}$ is an orthogonal matrix, then the Langevin dynamics Eq. (1) can be rewritten as

$$\tilde{\mathbf{x}}_t = \tilde{\mathbf{x}}_{t-1} + \frac{\epsilon_t^2}{2} \nabla_{\tilde{\mathbf{x}}} \log p_{\tilde{\mathbf{x}^*}}(\tilde{\mathbf{x}}_{t-1}) + \epsilon_t U \mathbf{z}_t, \quad (14)$$

where $\tilde{\mathbf{x}} = U \mathbf{x}$. Similarly, the reverse diffusion Eq.(12) can also be rewritten as

$$\tilde{\mathbf{x}}_t = \tilde{\mathbf{x}}_{t-1} + \bar{g}_t^2 \nabla_{\tilde{\mathbf{x}_t}} \log \bar{p}_t(\tilde{\mathbf{x}}_t) + \bar{g}_t U \mathbf{z}_t \quad (15)$$

Proof. Multiplying U at both sides of the original Langevin dynamics, we have

$$\tilde{\mathbf{x}}_{t-1} = \tilde{\mathbf{x}}_t + \frac{\epsilon_t^2}{2} U \nabla_{\mathbf{x}} \log p_{\mathbf{x}^*}(\mathbf{x}_t) + \epsilon_t U \mathbf{z}_t. \quad (16)$$

Using the change-of-variable technique, we have

$$p_{\tilde{\mathbf{x}^*}}(\tilde{\mathbf{x}}) = p_{\mathbf{x}^*}(U^{-1} \tilde{\mathbf{x}}) |U|^{-1}.$$

By taking the logarithm and calculating the gradients at both sides of the equation, we have

$$\nabla_{\tilde{\mathbf{x}}} \log p_{\tilde{\mathbf{x}}^*}(\tilde{\mathbf{x}}) = \nabla_{\tilde{\mathbf{x}}} \log p_{\mathbf{x}^*}(\mathbf{x}) \quad (17)$$

Combining Eq. (17), the chain rule $\nabla_{\mathbf{x}} = U^\top \nabla_{\tilde{\mathbf{x}}}$, and Eq. (16), we obtain

$$\tilde{\mathbf{x}}_{t-1} = \tilde{\mathbf{x}}_t + \frac{\epsilon_t^2}{2} UU^\top \nabla_{\tilde{\mathbf{x}}} \log p_{\tilde{\mathbf{x}}^*}(\tilde{\mathbf{x}}_t) + \epsilon_t U \mathbf{z}_t.$$

As U is orthogonal, $UU^\top = I_d$. We thus finish the proof for the Langevin dynamics Eq. (10). The proof of the reverse diffusion Eq. (12) is almost the same. \square

According to this theorem, we can directly transform the entire sampling process by an orthogonal transformation U , with the only difference that the noise is altered to $U \mathbf{z}_t$. Particularly, if \mathbf{z}_t obeys an isotropic Gaussian distribution applied by existing methods, $U \mathbf{z}_t$ obeys exactly the same distribution as \mathbf{z}_t . Hence, the sampling process is *orthogonally invariant*.

Since any permutation matrix is orthogonal, Eq. (10) ignores the coordinate order of data. This property could be suitable for unstructured data, but not for structured data (e.g., images) where the coordinate order represents the geometry information of individual pixels locally and the semantic structures globally.

3.5 Leveraging preconditioning

Conceptually, the Langevin dynamics Eq. (10) of the sampling process is a special case of Metropolis adjusted Langevin algorithm (MALA) [23], [24], [25] with non-autonomous factor ϵ_t . Inspired by the findings that the preconditioning approach can significantly accelerate the MALA [23], we study *how to construct a preconditioning operator M to accelerate the sampling phase of SGMs*.

Specifically, the original sample space may suffer from an ill-conditioned issue caused by the large variations of the scales in different coordinates. This could lead to oscillation and slow convergence, especially when the step size ϵ_t is not small enough [51]. Preconditioning can make the scales become more similar along all the coordinates [23], [26] using a *matrix preconditioner*, alleviating the ill-conditioned problem and improving the convergence of the sampling process even under a large step size. This applies to the reverse diffusion (Eq. (12)) similarly.

As shown in the following sections, with the proposed preconditioning, the noise terms \mathbf{z}_t become anisotropic (i.e., its covariance matrix is no longer a scalar matrix). As a result, the sampling process of SGMs is varying under the permutation of coordinates, becoming conditional to the coordinate order (Thm. 1).

4 THEORETICAL ANALYSIS

In this section, we develop the theories for the formulation of our preconditioning operator suitable for the predicting-correcting based sampling process (Alg. 1). As predicting and correcting can be applied in isolation for complete sampling [4], we will inspect them separately.

4.1 Continuous processes

For theoretical purposes, we first give the continuous version of sampling discussed in Sec. 3. The continuous version of Eq. (10) is

$$d\mathbf{x}_t = \frac{\epsilon_t^2}{2} \nabla_{\mathbf{x}_t} \log p_{\mathbf{x}^*}(\mathbf{x}_t) dt + \epsilon_t d\mathbf{w}_t, t \in [0, T] \quad (18)$$

starting from an initial distribution $\mathbf{x}_0 \sim \mathcal{N}(\mathbf{0}, I)$, with \mathbf{w}_t a Wiener process, and ϵ_t the continuous version of the step size. The continuous version for corrupting process (Eq. (11)) is

$$d\mathbf{x}_t = g_t d\mathbf{w}_t, t \in [0, T], \quad (19)$$

starting from an initial distribution $\mathbf{x}_0 \sim p_{\mathbf{x}^*}$. The continuous version of reverse diffusion (Eq. (12))

$$d\mathbf{x}_t = \bar{g}_t^2 \nabla_{\mathbf{x}} \log \bar{p}_t(\mathbf{x}_t) + \bar{g}_t d\mathbf{w}_t, t \in [0, T] \quad (20)$$

starting from an initial distribution $\mathbf{x}_0 \sim p_{\mathbf{x}^*}$. Note, with these processes, the distribution of the initial state \mathbf{x}_0 is different.

4.2 Preserving the steady-state distribution for the Langevin dynamics

To ensure the generation quality, the steady-state distribution of the Langevin dynamics (Eq. (18)) must stick with the target distribution $p_{\mathbf{x}^*}$; Otherwise, poor performance will be likely resulted. We prove that our preconditioning preserves the steady-state distribution.

We first derive the theory behind the Langevin dynamics on why it can generate samples from $p_{\mathbf{x}^*}$. According to [27], Eq. (18) is associated with a Fokker-Planck equation

$$\frac{\partial p}{\partial t} = -\frac{\epsilon_t^2}{2} \nabla_{\mathbf{x}} \cdot (\nabla_{\mathbf{x}} \log p_{\mathbf{x}^*}(\mathbf{x}_t) p) + \frac{\epsilon_t^2}{2} \Delta_{\mathbf{x}} p, \quad (21)$$

where $p = p(\mathbf{x}, t)$ is the distribution of \mathbf{x} at time t . This describes the stochastic dynamics of Eq. (18).

Let $\frac{\partial p}{\partial t} = 0$, we obtain the steady-state function

$$\nabla_{\mathbf{x}} \cdot (\nabla_{\mathbf{x}} \log p_{\mathbf{x}^*}(\mathbf{x}) p) = \Delta_{\mathbf{x}} p. \quad (22)$$

Its solution, i.e., the steady-state solution, corresponds to the probabilistic density function of the steady-state distribution of Eq. (18). Substituting p with $p_{\mathbf{x}^*}$ in Eq. (22), the L.H.S. of this equation becomes

$$\nabla_{\mathbf{x}} \cdot (\nabla_{\mathbf{x}} \log(p_{\mathbf{x}^*}) p_{\mathbf{x}^*}) = \nabla_{\mathbf{x}} \cdot (\nabla_{\mathbf{x}}(p_{\mathbf{x}^*})) = \Delta_{\mathbf{x}} p^*, \quad (23)$$

which is exactly the R.H.S. of the equation. Hence, the target data distribution $p_{\mathbf{x}^*}$ is one of the steady-state solutions of Eq. (18). It is proved that this steady-state solution is *unique*, s.t. $\epsilon_t > 0$ [52]. As a result, with enough iterations, the state distribution will converge to the target data distribution $p_{\mathbf{x}^*}$.

The Fokker-Planck equation indicates how to preserve the steady-state distribution of the original process under modification. Concretely, we can theoretically show that the steady-state distribution remains when changing Eq. (18) as

$$d\mathbf{x}_t = \frac{\epsilon_t^2}{2} (MM^\top + S) \nabla_{\mathbf{x}_t} \log p_{\mathbf{x}^*}(\mathbf{x}_t) dt + \epsilon_t M d\mathbf{w}_t, \quad (24)$$

where M is an invertible linear operator, S is any skew-symmetric operator, and M^\top is the adjoint operator of M .

Theorem 2. *The steady-state distribution of Eq. (24) is $p_{\mathbf{x}^*}$, as long as the linear operator M is invertible and the linear operator S is skew-symmetric.*

Proof. The invertibility of M preserves the uniqueness of the solution of the steady-state equation [27]. Hence we only need to prove that the target data distribution $p_{\mathbf{x}^*}$ still satisfies the steady-state equation after preconditioning. The Fokker-Planck equation of Eq. (24) is

$$\begin{aligned} \frac{\partial p}{\partial t} &= -\frac{\epsilon^2}{2} \nabla_{\mathbf{x}_t} \cdot (MM^T \nabla_{\mathbf{x}_t} \log p_{\mathbf{x}^*}(\mathbf{x})p) \\ &\quad - \frac{\epsilon^2}{2} \nabla_{\mathbf{x}_t} \cdot (S \nabla_{\mathbf{x}_t} \log p_{\mathbf{x}^*}(\mathbf{x})p) + \frac{\epsilon^2}{2} \nabla_{\mathbf{x}_t} \cdot (MM^T \nabla_{\mathbf{x}_t} p). \end{aligned}$$

The corresponding steady-state equation is

$$\begin{aligned} \nabla_{\mathbf{x}} \cdot (MM^T \nabla_{\mathbf{x}} \log p_{\mathbf{x}^*}(\mathbf{x})p) + \nabla_{\mathbf{x}} \cdot (S \nabla_{\mathbf{x}} \log p_{\mathbf{x}^*}(\mathbf{x})p) \\ = \nabla_{\mathbf{x}} \cdot (MM^T \nabla_{\mathbf{x}} p). \end{aligned}$$

Set $p = p_{\mathbf{x}^*}$, the above equation becomes

$$\begin{aligned} \nabla_{\mathbf{x}} \cdot (MM^T \nabla_{\mathbf{x}} \log(p_{\mathbf{x}^*})p_{\mathbf{x}^*}) + \nabla_{\mathbf{x}} \cdot (S \nabla_{\mathbf{x}} \log(p_{\mathbf{x}^*})p_{\mathbf{x}^*}) \\ = \nabla_{\mathbf{x}} \cdot (MM^T \nabla_{\mathbf{x}} p_{\mathbf{x}^*}). \end{aligned}$$

The first term in L.H.S. equals to the R.H.S., since

$$\nabla_{\mathbf{x}} \cdot (MM^T \nabla_{\mathbf{x}} p_{\mathbf{x}^*} \frac{1}{p_{\mathbf{x}^*}} p_{\mathbf{x}^*}) = \nabla_{\mathbf{x}} \cdot (MM^T \nabla_{\mathbf{x}} p_{\mathbf{x}^*}).$$

Additionally, the second term in the L.H.S. equals to

$$\nabla_{\mathbf{x}} \cdot (S \nabla_{\mathbf{x}} p_{\mathbf{x}^*}) = (\nabla_{\mathbf{x}} \cdot S \nabla_{\mathbf{x}}) p_{\mathbf{x}^*},$$

where the differential operator

$$\nabla_{\mathbf{x}} \cdot S \nabla_{\mathbf{x}} = \sum_{ij} \frac{\partial}{\partial x_i} \frac{\partial}{\partial x_j} S_{ij} = 0$$

since S is skew-symmetric. Therefore, the term $\nabla_{\mathbf{x}} \cdot (S \nabla_{\mathbf{x}} p_{\mathbf{x}^*}) = 0$. Then, the steady-state solution of Eq. (22), *i.e.*, $p_{\mathbf{x}^*}$, also satisfies the steady-state equation of Eq. (24). As a result, the theorem is proved. \square

Thm. 2 provides a wide manipulative space for us to design the preconditioning operator M and S while preserving the steady-state distribution of \mathbf{x}_T in the Langevin dynamics simultaneously.

4.3 Preserving the final-state distribution for the reverse diffusion

Unlike the Langevin dynamics, the reverse diffusion (Eq. (20)) directly reverses the corrupting process. So its final-steady state \mathbf{x}_T obeys $p_{\mathbf{x}^*}$ naturally [50]. Note the final-steady distribution of Eq. (20) may not be its steady-state distribution. This can be seen if we write out its steady-state equation through Fokker-Planck equation

$$2 \nabla_{\mathbf{x}} \cdot (\nabla_{\mathbf{x}} \log p_{\mathbf{x}^*}(\mathbf{x})p) = \Delta_{\mathbf{x}} p.$$

It is obvious that the target data distribution $p_{\mathbf{x}^*}$ does not satisfy this equation.

Accordingly, to enable the reverse diffusion generate samples from $p_{\mathbf{x}^*}$ after preconditioning, we must preserve its final-state distribution \mathbf{x}_T . To that end, we modify Eq. (20) as

$$d\mathbf{x}_t = \bar{g}_t^2 MM^T \nabla_{\mathbf{x}_t} \log \bar{p}_t(\mathbf{x}_t) + \bar{g}_t M d\mathbf{w}_t, t \in [0, T], \quad (25)$$

where M is an invertible linear operator. In fact, we have

Theorem 3. *The final-state distribution of Eq. (25) is also $p_{\mathbf{x}^*}$, subject to M is an invertible linear operator.*

Proof. Denote $p_{\mathbf{y}^*}$ as the probabilistic distribution function of $\mathbf{y} = M^{-1}\mathbf{x}$, where $\mathbf{x} \sim p_{\mathbf{x}^*}$. We consider the corrupting process for $p_{\mathbf{y}^*}(\mathbf{y})$. Define the transformed corrupting process (starting from $\mathbf{y}_0 \sim p_{\mathbf{y}^*}$)

$$d\mathbf{y}_t = M^{-1}d\mathbf{w}_t, t \in [0, T], \quad (26)$$

Denote $\tilde{p}_t(\mathbf{y})$ as the probabilistic distribution function of the \mathbf{y}_{T-t} in the process Eq. (26). Denote $\mathbf{y}_t = M^{-1}\mathbf{x}_t$, and substituting \mathbf{y}_t into Eq. (25), we have

$$d\mathbf{y}_t = \bar{g}_t^2 M^T \nabla_{\mathbf{x}_t} \log \bar{p}_t(\mathbf{x}_t) + \bar{g}_t d\mathbf{w}_t, t \in [0, T], \quad (27)$$

where we have operated M^{-1} at both sides of the equation and use the relation $\mathbf{y} = M^{-1}\mathbf{x}$. We show that Eq. (27) is the reverse process of Eq. (26). With the change-of-variable relationship of the probabilistic distribution function

$$\bar{p}_t(\mathbf{x}_t) = \tilde{p}_t(\mathbf{y}_t) |\det [M^{-1}]|, \quad (28)$$

and the chain rule $\nabla_{\mathbf{x}_t} = M^{-T} \nabla_{\mathbf{y}_t}$ we have

$$M^{-T} \nabla_{\mathbf{x}_t} \log \bar{p}_t(\mathbf{x}_t) = \nabla_{\mathbf{y}_t} \log \tilde{p}_t(\mathbf{y}_t). \quad (29)$$

In Eq. (28), M^{-1} is considered as a matrix, and $\det [M^{-1}]$ is its discriminant. Therefore, Eq. (27) can be written as

$$d\mathbf{y}_t = \bar{g}_t^2 \nabla_{\mathbf{y}_t} \log \tilde{p}_t(\mathbf{y}_t) + \bar{g}_t d\mathbf{w}_t, t \in [0, T],$$

which is exactly the reverse process of Eq. (26) [50]. As a result, the final-state distribution of Eq. (27) obeys $\mathbf{y}_T \sim p_{\mathbf{y}^*}$. Reversing M on Eq. (27), the final-state distribution of Eq. (25) thus obeys $\mathbf{x}_T \sim p_{\mathbf{x}^*}$. \square

Similar as Thm. 2, Thm. 3 provides a wide space for designing the preconditioner M while preserving the final-state distribution of \mathbf{x}_T in the reverse diffusion.

5 PRECONDITIONED DIFFUSION SAMPLING

Thus far, we have presented the generic preconditioning formulation for both Langevin dynamics and reverse diffusion. Next, we focus on image generation tasks by designing proper operators.

5.1 Image preconditioning strategies

In numerical optimization, accurate preconditioning operators could be obtained by calculating the inverse of the Hessian matrix of $\log p_{\mathbf{x}^*}(\mathbf{x})$ at each time step. This however is extremely costly for high dimensional tasks (*e.g.*, image generation) [53]. To bypass this obstacle, we adopt a data-centred strategy that leverages the per-coordinate scale information of target data.

For imagery data, we consider two types of coordinate: individual pixels (*i.e.*, the spacial coordinate) and frequency (*i.e.*, Fourier transformed). The former is useful for images with global structure characteristics, as per-pixel statistics gives prior information (*i.e.*, **pixel preconditioner**). With natural images, the amplitude of low-frequency components is typically much higher than that of high-frequency ones [54]. This structural frequency property could be similarly useful.

(*i.e.*, *frequency preconditioner*). For either case, we construct the linear operator M with the mean value of target training data, used to balance all the coordinates (Fig. 2). We simply set the skew-symmetric operator S (Eq. (24)) as zero and will discuss it later.

Combining the two preconditioners, we form a linear preconditioning operator $M \in \mathbb{R}^d \rightarrow \mathbb{R}^d$ as $M[\cdot] = M_f[M_p[\cdot]]$ with M_f and M_p the preconditioner for frequency and pixel, respectively. We operate M on the noise term \mathbf{z}_t and adjust the gradient term to keep the steady-state distribution for the Langevin dynamics Eq. (10) as

$$\begin{aligned} \mathbf{x}_t &= \mathbf{x}_{t-1} + \frac{\epsilon_t^2}{2} M_p[M_f^2[M_p[\nabla_{\mathbf{x}} \log p_{\mathbf{x}^*}(\mathbf{x}_{t-1})]]] \\ &+ \epsilon_t M_f[M_p[\mathbf{z}_t]], 1 \leq t \leq T. \end{aligned} \quad (30)$$

Similarly, we preserve the final-state distribution for the reverse diffusion Eq. (20) as

$$\begin{aligned} \mathbf{x}_t &= \mathbf{x}_{t-1} + \bar{g}_t^2 M_p[M_f^2[M_p[\nabla_{\mathbf{x}} \log \bar{p}_t(\mathbf{x}_{t-1})]]] \\ &+ \bar{g}_t M_f[M_p[\mathbf{z}_t]], 1 \leq t \leq T, \end{aligned} \quad (31)$$

We called this proposed sampling procedure as *preconditioned diffusion sampling* (PDS), as summarized in Alg. 2.

Algorithm 2 Preconditioned diffusion sampling (PDS)

Input: The frequency M_f and pixel M_p preconditioner, the sampling iterations T , the model \mathbf{s}_θ .

Defining the preconditioning operator $M[\cdot] = M_f[M_p[\cdot]]$
Drawing $\mathbf{x}_0 \sim \mathcal{N}(\mathbf{0}, I)$

for $t = 1$ **to** T **do**

Predicting (reverse diffusion):

 Drawing $\mathbf{z}_t \sim \mathcal{N}(\mathbf{0}, I)$

$\mathbf{x}'_t \leftarrow \mathbf{x}_{t-1} + \bar{g}_t^2 M[M^T[\mathbf{s}_\theta(\mathbf{x}_{t-1}, \bar{g}_t)]] + \bar{g}_t M[\mathbf{z}_t]$

Correcting (Langevin dynamics):

 Drawing $\mathbf{z}_t \sim \mathcal{N}(\mathbf{0}, I)$

$\mathbf{x}_t \leftarrow \mathbf{x}'_t + \frac{\epsilon_t^2}{2} M[M^T[\mathbf{s}_\theta(\mathbf{x}'_t, \epsilon_t)]] + \epsilon_t M[\mathbf{z}_t]$

end for

Output: \mathbf{x}_T

5.2 Constructing image preconditioners

In this section, we design the frequency M_f and pixel M_p preconditioners. We denote an image training dataset $\mathcal{D} = \{\mathbf{x}^{(i)} \in \mathbb{R}^{C \times H \times W}, i = 1, \dots, N\}$, where C , H and W are the channel number, height and width of images, respectively.

5.2.1 Frequency preconditioner M_f

Using the frequency statistics of the training set, we design the frequency preconditioner M_f as

$$M_f[\mathbf{x}] = F^{-1}[F[\mathbf{x}] \bullet R_f], \quad \forall \mathbf{x} \in \mathbb{R}^{C \times W \times H} \quad (32)$$

where F is Discrete Fourier Transform, \bullet the element-wise division and the frequency mask $R_f \in \mathbb{R}^{C \times W \times H}$ defined as

$$R_f = \log(\mathbb{E}_{\mathbf{x} \sim p^*(\mathbf{x})} [F[\mathbf{x}] \odot \overline{F[\mathbf{x}]}] + 1) \quad (33)$$

where \odot is the element-wise multiplication. For better stability, we further normalize the mask as

$$R_f(c, w, h) \leftarrow \frac{1}{\alpha} \left(\frac{R_f(c, w, h)}{\max_{c, w, h} R_f(c, w, h)} + \alpha - 1 \right), \quad (34)$$

where $\alpha \in [1, +\infty)$ is the normalization parameter. The intuition is that, the mask M_f shrinks the frequency coordinates with larger scales more than the others, so that the scales of all coordinates can become similar. This mitigates the ill-conditioned issue in the frequency space as mentioned earlier.

5.2.2 Pixel preconditioner M_p

With the pixel statistics, we similarly design the pixel preconditioner M_p that operates in the pixel space as follows:

$$M_p[\mathbf{x}] = \mathbf{x} \bullet R_p, \quad \forall \mathbf{x} \in \mathbb{R}^{C \times W \times H} \quad (35)$$

with the pixel mask $R_p \in \mathbb{R}^{C \times W \times H}$ defined as

$$R_p = \log(\mathbb{E}_{\mathbf{x} \sim p^*(\mathbf{x})} [\mathbf{x} \odot \mathbf{x}] + 1). \quad (36)$$

We also apply normalization as

$$R_p(c, h, w) \leftarrow \frac{1}{\alpha} \left(\frac{R_p(c, h, w)}{\max_{c, h, w} R_p(c, h, w)} + \alpha - 1 \right) \quad (37)$$

with the normalization parameter α same as in Eq. (34).

For the tasks without clear pixel structure characteristics, we do not apply this pixel preconditioner by setting all the elements of R_p to 1 (*i.e.*, an identity operator).

5.2.3 Computational complexity

Only a small set of images are needed to estimate the statistics for Eq. (33) and Eq. (36). In practice, we use 200 random images with marginal cost. For the computational complexity of PDS during sampling, the major overhead is from FFT [28] and its inverse with the complexity of $O(CHW(\log H + \log W)) = O(d(\log H + \log W))$. This is neglectable w.r.t the original cost (see Table 5).

6 FURTHER ANALYSIS

6.1 Gradient descent perspective

We can understand the preconditioning on the Langevin dynamics from the gradient descent perspective. Given the target data distribution $p_{\mathbf{x}^*}$, we define the energy function (a.k.a. surprise in cognitive science [55])

$$E(\mathbf{x}) = -\log p_{\mathbf{x}^*}(\mathbf{x}), \quad \forall \mathbf{x} \in \mathbb{R}^d \quad (38)$$

Substituting the definition of E into Eq. (10), we have

$$\mathbf{x}_t = \mathbf{x}_{t-1} - \frac{\epsilon_t^2}{2} \nabla_{\mathbf{x}} E(\mathbf{x}_{t-1}) + \epsilon_t \mathbf{z}_t, 1 \leq t \leq T. \quad (39)$$

Clearly, the Langevin dynamics is implementing the gradient descent algorithm for minimizing the energy of the sample point \mathbf{x}_t , along with an additive noise term \mathbf{z}_t . This optimizer is called stochastic gradient Langevin dynamics (SGLD) [24]. Unlike stochastic gradient descent, the randomness of SGLD comes from the noise \mathbf{z}_t , instead of drawing from the training set. Besides, SGLD sequentially reduce the energy ($-\log p_{\mathbf{x}^*}(\mathbf{x})$) of a sample \mathbf{x}_t via SGLD.

6.2 Skew-symmetric operator

In the gradient descent perspective, $S \nabla_{\mathbf{x}} E(\mathbf{x}_{t-1})dt$ of Eq. (24) is known as solenoidal term, since it corresponds to the direction along which the energy does not change (*i.e.*, $\langle \nabla_{\mathbf{x}} E(\mathbf{x}_{t-1}), S \nabla_{\mathbf{x}} E(\mathbf{x}_{t-1}) \rangle = 0$). Seemingly it imposes no effect on acceleration. But several studies [56], [57], [58], [59] suggest that it can help reach the steady state distribution faster.

For completeness, we discuss the possibility of the skew-symmetric operator S as an accelerator for the Langevin dynamics. According to [56], under the regularity condition that $|\mathbf{x}_t|$ does not reach the infinity in a finite time, the convergence of an *autonomous* (the right side of the equation does not contain time explicitly) Langevin dynamics

$$d\mathbf{x}_t = \frac{\epsilon_t^2}{2} \nabla_{\mathbf{x}_t} \log p_{\mathbf{x}^*}(\mathbf{x}_t)dt + \epsilon_t d\mathbf{w}_t, \quad (40)$$

where $\epsilon_t = \epsilon$ is a constant, can be accelerated as

$$d\mathbf{x}_t = \frac{\epsilon_t^2}{2} \nabla_{\mathbf{x}_t} \log p_{\mathbf{x}^*}(\mathbf{x}_t)dt + C(\mathbf{x}_t)dt + \epsilon_t d\mathbf{w}_t, \quad (41)$$

where the vector field $C(\mathbf{x}) \in \mathbb{R}^d \rightarrow \mathbb{R}^d$ satisfies

$$\nabla_{\mathbf{x}} \cdot \left(\frac{C(\mathbf{x})}{p_{\mathbf{x}^*}(\mathbf{x})} \right) = 0. \quad (42)$$

$C(\mathbf{x}) = S \nabla_{\mathbf{x}} \log p_{\mathbf{x}^*}(\mathbf{x})$ satisfies the above condition. However, the Langevin dynamics of existing SGMs is typically *not autonomous*, as the step size ϵ_t varies across time. Despite this, it is still worth investigating the effect of S (see Sec. 7).

6.3 Parameter selection

We investigate how to set properly α of Eq. (37) and Eq. (34). Increasing α will weaken the preconditioning effect; When $\alpha \rightarrow +\infty$, M_f and M_p both become the identity operator. Empirically, we find that for higher iterations T , higher α is preferred (Table 1). We aim to quantify the relation between α and T .

By Thm. 3, the preconditioned reverse diffusion (Eq. (31)) reverses the transformed forward process (Eq. (26)), instead of the original one (Eq. (19)) used in model training. The deviation between Eq. (26) and Eq. (19) brings challenge for the model to fit the score function, as the noisy input distribution deviates from what is exposed to model training at each step. We assume the error per iteration grows linearly with this deviation, proportional to

$$\|M_p[M_f[\cdot]] - I[\cdot]\|, \quad (43)$$

where I is the identity operator, and $\|\cdot\|$ is the l_2 norm of the linear operators in $\mathbb{R}^d \rightarrow \mathbb{R}^d$.

With Eq. (34) and (37), in case of large

$$M_f(\alpha) \sim I + O\left(\frac{1}{\alpha}\right)I, \quad M_p(\alpha) \sim I + O\left(\frac{1}{\alpha}\right)I. \quad (44)$$

By design, the elements of R_f (Eq. (33)) and R_p (Eq. (36)) vary moderately. Thus the accumulated error of the whole sampling process is $O(T \|M_p[M_f[\cdot]] - I[\cdot]\|)$. With Eq. (44), this error scale can be written

$$T\sqrt{d}\left[\left(1 + O\left(\frac{1}{\alpha}\right)\right)\left(1 + O\left(\frac{1}{\alpha}\right)\right) - 1\right]. \quad (45)$$

Omitting high order terms, it could be simplified as

$$T\sqrt{d}\left[\left(1 + O\left(\frac{1}{\alpha}\right)\right)\left(1 + O\left(\frac{1}{\alpha}\right)\right) - 1\right] = O(1), \quad (46)$$

This implies that there exists constants c_1, c_2, a and b ($c_1, c_2, a \neq 0$) independent from α and T such that

$$\left(1 + \frac{c_1}{\alpha}\right)\left(1 + \frac{c_2}{\alpha}\right) - 1 = a\frac{1}{T} + b, \quad (47)$$

In case of only applying the frequency preconditioner M_f , Eq. (46) becomes

$$T\sqrt{d}\left[1 + O\left(\frac{1}{\alpha}\right) - 1\right] = O(1), \quad (48)$$

and the corresponding linear relation is

$$\left(1 + \frac{c_1}{\alpha}\right) - 1 = a\frac{1}{T} + b. \quad (49)$$

After quantifying this relation by searching the optimal α for only a couple of different T , we can directly estimate α for any other T without manual search.

7 EXPERIMENTS

In this section, we first show that PDS can accelerate the sampling process of the state-of-the-art SGMs while maintaining the sampling quality and provide parameter analysis. We use CIFAR-10 [60], CelebA [61] at a resolution of 64×64 , LSUN (bedroom and church) [62] at a resolution of 256×256 , and FFHQ [21] at a resolution of 1024×1024 . Note that for all these datasets, the image height and width are identical, *i.e.*, $H = W$. The CelebA and FFHQ datasets are human facial images, with strong pixel-wise structural characteristics. For them, we hence apply both frequency and pixel filter for these two datasets. For other datasets, we only apply the frequency preconditioner. We adopt the same preprocessing as [4]. We evaluate PDS on the state-of-art SGM *i.e.*, NCSN++ [4]. For fair comparison, we only replace the vanilla sampling method (Alg. 1) with our PDS (Alg. 2) whilst keeping the remaining unchanged during inference for a variety of sampling iterations, without model retraining and other alteration. Whenever reducing the iterations from the original one T to T/c with a factor c we simultaneously expand the step size from the original one ϵ_t to $\sqrt{c}\epsilon_t$ for $t = 1, \dots, T$ for consistent accumulative update of the score function and consistent variance of the added noises. We use the public codebase of [4]. We use the released checkpoints for all SGMs except NCSN++ on CelebA (64×64), for which no released checkpoint, and we train by ourselves with the released codes instead.

7.1 Evaluating on sampling quality

We show that PDS can accelerate the sampling process of SGMs (NCSN++) for generating samples on datasets across various resolutions. See Table 1 the setting of parameter α for different iterations T by our linear relation (Sec. 6.3).

CIFAR-10 and CelebA. In Table 2 and Table 3, we evaluate the PDS with NCSN++ on CIFAR-10 (32×32) and CelebA (64×64) under various iterations T . We use FID [63] score as metric. We compare PDS with representative DDPMs

TABLE 1: Parameters α of PDS used for constructing preconditioner on NCSN++ [4] under different iterations T .

| Iterations T | Dataset | |
|----------------|----------|---------------------------|
| | CIFAR-10 | CelebA (64×64) |
| 1000 | 50 | 300 |
| 400 | 25 | 40 |
| 200 | 12 | 15 |
| 100 | 5 | 6 |
| 50 | 1.8 | 2.5 |

(DDPM [35], DDIM [30], Analytic-DDPM [31], Analytic-DDIM [31], and PNDM [38]). We provide visual samples on CIFAR-10 and CelebA in Appendix.

Although achieving on-par performance with DDPMs given large iterations, NCSN++ degrades more significantly as the iteration decreases. This can be solved by our PDS whilst further improving large-iteration performance and achieving the best results in most low-iteration cases. As shown in Table 4, our PDS achieves a FID score of 1.99 on CIFAR-10, surpassing prior GANs, DDPMs and SGMs.

LSUN [62]. We test PDS with NCSN++ to generate bedroom and church images at a resolution of 256×256 . As shown in Fig. 3, our PDS can prevent the output images from being ruined by heavy noises under low iterations. See more visualization in Appendix.

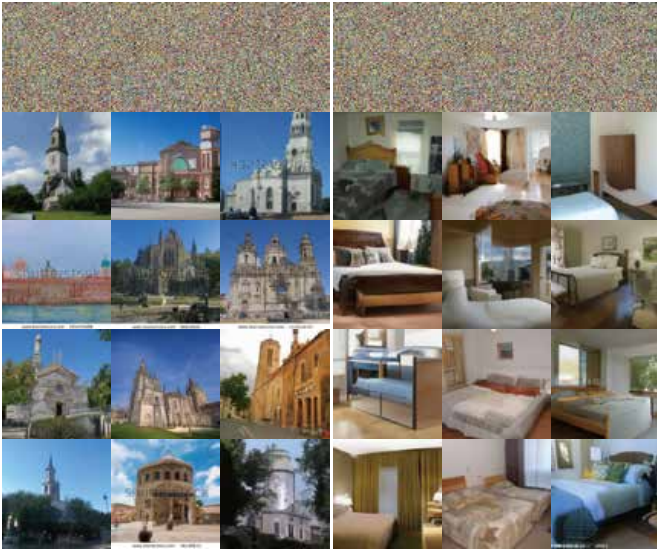


Fig. 3: Sampling on LSUN (church and bedroom) (256×256). **Top:** NCSN++ [4] **Bottom:** NCSN++ with PDS. Both use 80 iterations and $\alpha = 2.2$. More samples in Appendix.

FFHQ [21]. We further test PDS to generate high-resolution facial images at a resolution of 1024×1024 . Similarly under acceleration the original sampling method suffers from heavy noises and fails to produce recognizable human faces. Our PDS maintains the sampling quality using as few as 66 iterations (Fig. 1 and Fig. 10). **ImageNet [67] and COCO [68].** We further investigate the effect of PDS on NCSN++ in generating samples on ImageNet and COCO respectively. As the first ImageNet and COCO evaluation for VE-SDE models, we train a NCSN++ [4] by ourselves at the resolution of 64×64 as the baseline.

We apply the same hyper-parameters of optimizer and learning schedule as [4]. We train the model for 110k iterations for ImageNet and 600k for COCO. The batch size is set at 256 for both datasets. As shown in Fig. 4, our PDS yields consistently acceleration effect across a variety of sampling iterations. We show image samples in Fig. 7 and Fig. 8 of Appendix.

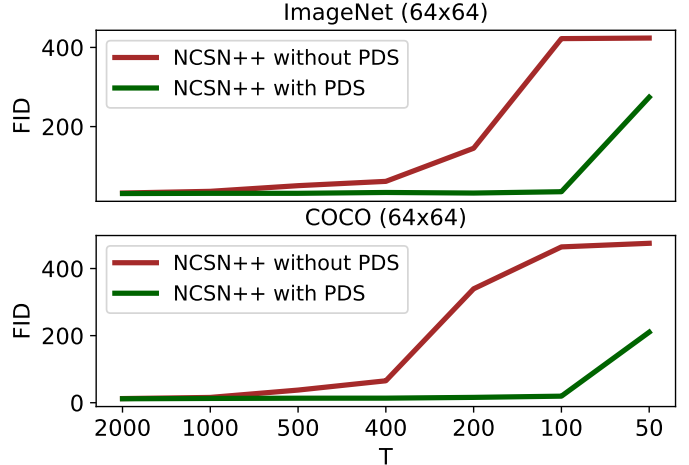


Fig. 4: The FID score of NCSN++ [4] with and without PDS on ImageNet and COCO under various iterations T .

7.2 Evaluation on running speed

We evaluate the effect of running speed from using PDS. In this test, we use one NVIDIA RTX 3090 GPU. We track the average wall-clock time of generating a batch of 8 images. As shown in Table 5, PDS only introduces marginal extra time complexity per iteration, corroborating our complexity analysis in Sec. 5.2.3. Importantly, PDS enables low-iteration generation for better efficiency. For example, for the high-resolution generation task on FFHQ (1024), PDS reduces the time cost of generating 8 human facial samples from 1920 to 68 in seconds, *i.e.*, $28 \times$ speedup.

TABLE 5: Comparing the running time *per iteration* of generating a batch of 8 images. *Time unit:* Seconds.

| Dataset Resolution | CelebA 64×64 | LSUN 256×256 | FFHQ 1024×1024 |
|-----------------------|--------------------------|--------------------------|----------------------------|
| NCSN++ [4] | 0.10 | 0.51 | 0.96 |
| NCSN++ w/ PDS | 0.12 | 0.54 | 1.03 |

7.3 Relation between α and T

The linear relation between α and T , as derived in Sec. 6.3, can ease the estimation of α for different T . To quantify this, we just need to search the optimal α for two different T . To simplify Eq. (47) and (49) we set $c_1 = c_2 = 1$ and have

$$\left(1 + \frac{1}{\alpha}\right)^2 - 1 = a_2 \frac{1}{T} + b_2, \quad \left(1 + \frac{1}{\alpha}\right) - 1 = a_1 \frac{1}{T} + b_1. \quad (50)$$

We test CIFAR-10 with only the frequency preconditioner and CelebA, ImageNet, and COCO (64×64) with both. The results of linear regression are depicted in Fig. 5. We obtain

TABLE 2: FID scores under different iterations T on CIFAR-10.

| Iterations T | NCSN++ [4] | NCSN++ w/ PDS | DDPM [35] | DDIM [30] | Analytic-DDPM [31] | Analytic-DDIM [31] | PNDM [38] |
|----------------|------------|---------------|-----------|-----------|--------------------|--------------------|-------------|
| 50 | 306.91 | 4.90 | 66.28 | 7.74 | 7.25 | 4.04 | 3.95 |
| 100 | 29.39 | 2.90 | 31.36 | 6.08 | 5.40 | 3.55 | 3.72 |
| 200 | 4.35 | 2.53 | 12.96 | 5.07 | 4.01 | 3.39 | 3.48 |
| 400 | 2.40 | 2.19 | 4.86 | 4.61 | 3.62 | 3.50 | 3.57 |
| 1000 | 2.23 | 1.99 | 3.17 | 4.13 | 4.03 | 3.74 | 3.70 |

TABLE 3: FID scores under different iterations T on CelebA (64×64).

| Iterations T | NCSN++ [4] | NCSN++ w/ PDS | DDPM [35] | DDIM [30] | Analytic-DDPM [31] | Analytic-DDIM [31] | PNDM [38] |
|----------------|------------|---------------|-----------|-----------|--------------------|--------------------|-------------|
| 50 | 438.84 | 13.48 | 115.69 | 9.33 | 11.23 | 6.13 | 5.69 |
| 100 | 433.98 | 3.49 | 25.65 | 6.60 | 8.08 | 4.29 | 4.03 |
| 200 | 292.51 | 3.21 | 9.72 | 4.96 | 6.51 | 3.46 | 3.04 |
| 400 | 7.09 | 2.95 | 3.95 | 4.15 | 5.87 | 3.38 | 3.07 |
| 1000 | 3.33 | 3.25 | 3.16 | 3.40 | 5.21 | 3.13 | 2.99 |

TABLE 4: FID comparison on CIFAR-10.

| Type | Method | FID |
|------|--------------------|-------------|
| GAN | BigGAN [64] | 14.73 |
| | StyleGAN2-ADA [65] | 2.42 |
| DDPM | DDPM [35] | 3.17 |
| | DDIM [30] | 4.13 |
| | Analytic-DDPM [31] | 3.63 |
| | Analytic-DDIM [31] | 3.39 |
| | PNDM [38] | 3.26 |
| | DDPM++ [4] | 2.91 |
| SGM | NCSN++ [4] | 2.23 |
| | CLD-SGM [29] | 2.23 |
| | LSGM [34] | 2.10 |
| | INDM [66] | 2.28 |
| | NCSN++ w/ PDS | 1.99 |

the coefficient of determination of 0.895 on CIFAR-10, 0.940 on CelebA(64×64), 0.992 on ImageNet (64×64), and 0.804 respectively. This suggests strong linear relations, validating our analysis. Note, when $(1 + \frac{1}{\alpha})^2 - 1$ and $(1 + \frac{1}{\alpha}) - 1$ are similar, the ratio of the slope a will be close to the square root of the dimension ratio. For instance, the relation between CIFAR-10 and CelebA(64×64) fits as:

$$\frac{a_1}{a_2} = \frac{28.53}{50.67} = 0.56 \sim 0.5 = \sqrt{\frac{3 \times 32 \times 32}{3 \times 64 \times 64}} = \sqrt{\frac{d_1}{d_2}}, \quad (51)$$

where a_1, a_2 are the slopes, and d_1, d_2 are their dimensions for CIFAR-10, CelebA (64×64), and ImageNet (64×64), respectively.

7.4 Sensitivity of parameters

We evaluate the parameter sensitivity of PDS. We perturb the optimal α (Table 1) by $\pm 10\%$. As shown in Table 6, the performance is not parameter-sensitive.

TABLE 6: Parameter (α) sensitivity analysis on CIFAR-10.

| Iterations T | before perturbation | +10% | -10% |
|----------------|---------------------|------|------|
| 1000 | 1.99 | 2.00 | 2.01 |
| 500 | 2.11 | 2.13 | 2.12 |
| 400 | 2.19 | 2.20 | 2.19 |
| 200 | 2.53 | 2.56 | 2.58 |
| 100 | 2.90 | 3.16 | 3.10 |
| 50 | 4.90 | 5.45 | 7.34 |

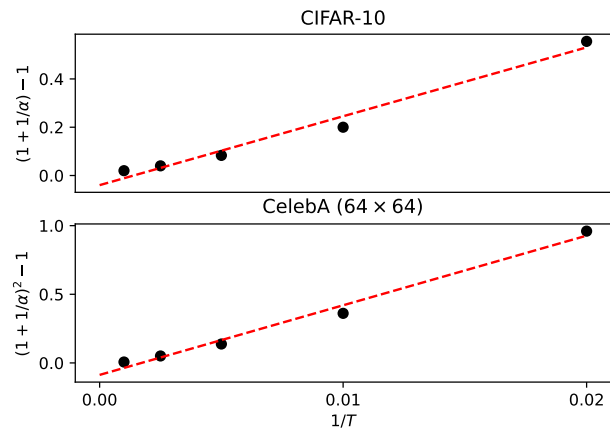


Fig. 5: The relation between the iterations T and the parameter α , both suggesting strong linear correlation.

7.5 Evaluating the skew-symmetric operator

We study the effect of the solenoidal term $S \nabla_{\mathbf{x}} \log p_{\mathbf{x}^*}(\mathbf{x}) dt$ to the Langevin dynamics. As proved in Thm. 2, as long as S is skew-symmetric, it will not change the steady-state distribution of the original process. To verify this, we generalize the original process as

$$d\mathbf{x}_t = \frac{\epsilon_t^2}{2} (MM^T + \omega S) \nabla_{\mathbf{x}_t} \log p_{\mathbf{x}^*}(\mathbf{x}_t) dt + \epsilon_t M d\mathbf{w}_t,$$

where ω controls the weight of S . We experiment with $S[\cdot] = \text{Re}[F[\cdot] - F^T[\cdot]]$ for being skew-symmetric and $\omega \in [1, 1000]$. Fig. 6 shows that ω has no impact to the generation quality. This verifies that S does not change the steady-state distribution of the original Langevin dynamics.

We further perform similar tests with different iterations

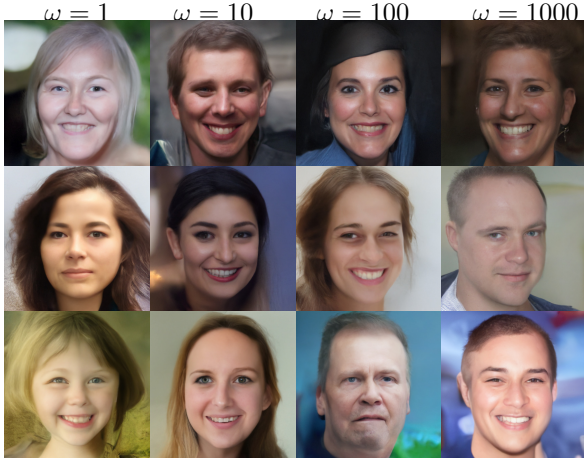


Fig. 6: Samples produced by NCSN++ [4] w/ PDS on FFHQ (1024x1024) with different solenoidal terms. Iterations: 66.

and other different skew-symmetric operator S :

$$S_1 = P_{1,1} - P_{1,1}^T \quad (52)$$

$$S_2 = P_{10,10} - P_{10,10}^T \quad (53)$$

$$S_3 = P_{100,100} - P_{100,100}^T \quad (54)$$

$$S_4 = \text{Re}[F[P_{1,1} - P_{1,1}^T]F^{-1}] \quad (55)$$

$$S_5 = \text{Re}[F[P_{10,10} - P_{10,10}^T]F^{-1}] \quad (56)$$

$$S_6 = \text{Re}[F[P_{100,100} - P_{100,100}^T]F^{-1}], \quad (57)$$

where $P_{m,n}$ is the shift operator that rolls the input image for m places along the height coordinate and rolls the input image for n places along the width coordinate. The sampling results are shown in Fig. 9, where we set $\omega = 1000$. It is observed that again all these solenoidal terms do not impose an obvious effect on the sampling quality. Additionally, as displayed in Fig. 15 in the supplementary material, these solenoidal terms also do not make an obvious effect on acceleration. We leave more extensive study of the solenoidal terms in the further work.

7.6 Experiments on other SGMs

We evaluate the performance of PDS on two more SGMs, *i.e.*, NCSN [2] and NCSNv2 [3]. Although the approach of constructing preconditioning operators in Sec. 5.2 works well for accelerating NCSN++ [4], it is less effective for NCSN [2] and NCSNv2 [3]. A possible reason is that the two models are less capable of exploiting the data statistics. To address this, we construct a simpler version of frequency preconditioner as

$$R_f(c, h, w) = \begin{cases} 1, & \text{if } (h - 0.5H)^2 + (w - 0.5W)^2 \leq 2r^2 \\ \lambda, & \text{if } (h - 0.5H)^2 + (w - 0.5W)^2 > 2r^2 \end{cases}, \quad (58)$$

where C is the channel number, H is the height, and W is the width of an image. $1 \leq c \leq C$, $1 \leq h \leq H$ and $1 \leq w \leq W$. The parameter $\lambda > 0$ specifies the ratio for scaling the frequency coordinates located out of the area $\{(h - 0.5H)^2 + (w - 0.5W)^2 \leq 2r^2\}$. The radial range of the area is controlled by r . See an illustration of the R_f in Fig. 8.

We do not normalize R_f and directly use it for constructing the corresponding preconditioning operator

$$M_f[\mathbf{x}] = F^{-1}[F[\mathbf{x}] \bullet R_f]. \quad (59)$$

Note that for NCSN and NCSNv2 have only corrector in the sampling process. We set λ so that the operator M_f balances the coordinates of low and high frequency components of its input via shrinking the scale of low-frequency coordinates. This is because that the scale of low-frequency coordinates is higher than that of high-frequency coordinates among natural images [54]. As shown in Fig. 1-3 in Appendix Fig. 4, PDS can dramatically accelerate the sampling process of NCSN on MNIST that of NCSNv2 on LSUN.

7.7 Compared with subspace diffusion generative models (SDGMs)

The subspace diffusion generative models (SDGMs) [45] restrict the sampling process of the SGMs on a low-dimensional subspace for acceleration. This might also help to mitigate the issue of ill-conditioning. We thus compare our PDS with SDGMs in terms of the effect of alleviating ill-conditioning.

We conduct two separate experiments to evaluate their performance. In the first experiment, we investigate the performance of two methods in terms of varying iterations. As shown in Table 7, our PDS achieves lower/better FID scores when compared to SDGMs subject to the same iterations. It is important to highlight that SDGM benefits from a smaller per-iteration cost due to reduced dimensionality, allowing it to execute more iterations within the same runtime. Hence we conduct a second experiment with a comparison taking into account the runtime and sample quality of the two methods, aiming to maintain a different fair evaluation. As depicted in Fig. 7, our PDS demonstrates the ability to generate higher-quality images (as indicated by a lower FID score) at the equivalent runtime cost when compared to SDGMs. In summary, our preconditioning strategy surpasses the dimension reduction idea of SDGM.

| Iterations T | 50 | 100 | 200 | 400 | 500 | 1000 |
|----------------|--------|-------|------|------|------|------|
| PDS | 4.90 | 2.90 | 2.53 | 2.19 | 2.11 | 1.99 |
| SDGM | 386.70 | 64.05 | 7.03 | 3.03 | 2.70 | 2.17 |

TABLE 7: Comparison of our PDS and SDGM [45] on CIFAR-10 generation under varying iterations.

8 CONCLUSION

We have proposed a novel preconditioned diffusion sampling (PDS) method for accelerating off-the-shelf score-based generative models (SGMs), without model retraining. Considering the sampling process as a combination of Langevin dynamics and reverse diffusion, we reveal that existing sampling suffers from the ill-conditioned issue. To solve this, we reformulate both the Langevin dynamics and the reverse diffusion with statistics based matrix preconditioning. Theoretically, PDS preserves the steady-state (*i.e.*, target) distribution of the Langevin dynamics and the final-state distribution of the reverse diffusion respectively. We

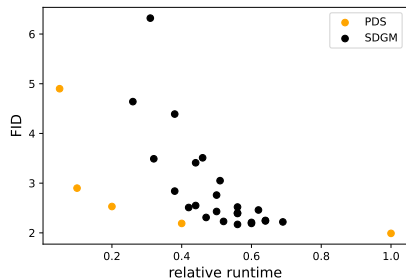


Fig. 7: Comparison of our PDS and SDGM [45] on CIFAR-10 generation. We report the FID score and the corresponding relative runtimes. Relative runtime is with respect to the vanilla SGM.

show that PDS significantly accelerates existing state-of-the-art SGMs while maintaining the generation quality, matching or even surpassing representative SGMs and DDPMs.

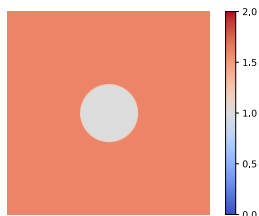


Fig. 8: Examples of frequency preconditioning R_f with $(r, \lambda) = (0.1H, 1.6)$ in Eq. (59).



Fig. 9: Facial images generated by NCSN++ [4] with our PDS using different solenoidal items. Iterations T : 66. Dataset: FFHQ [21] (1024×1024).

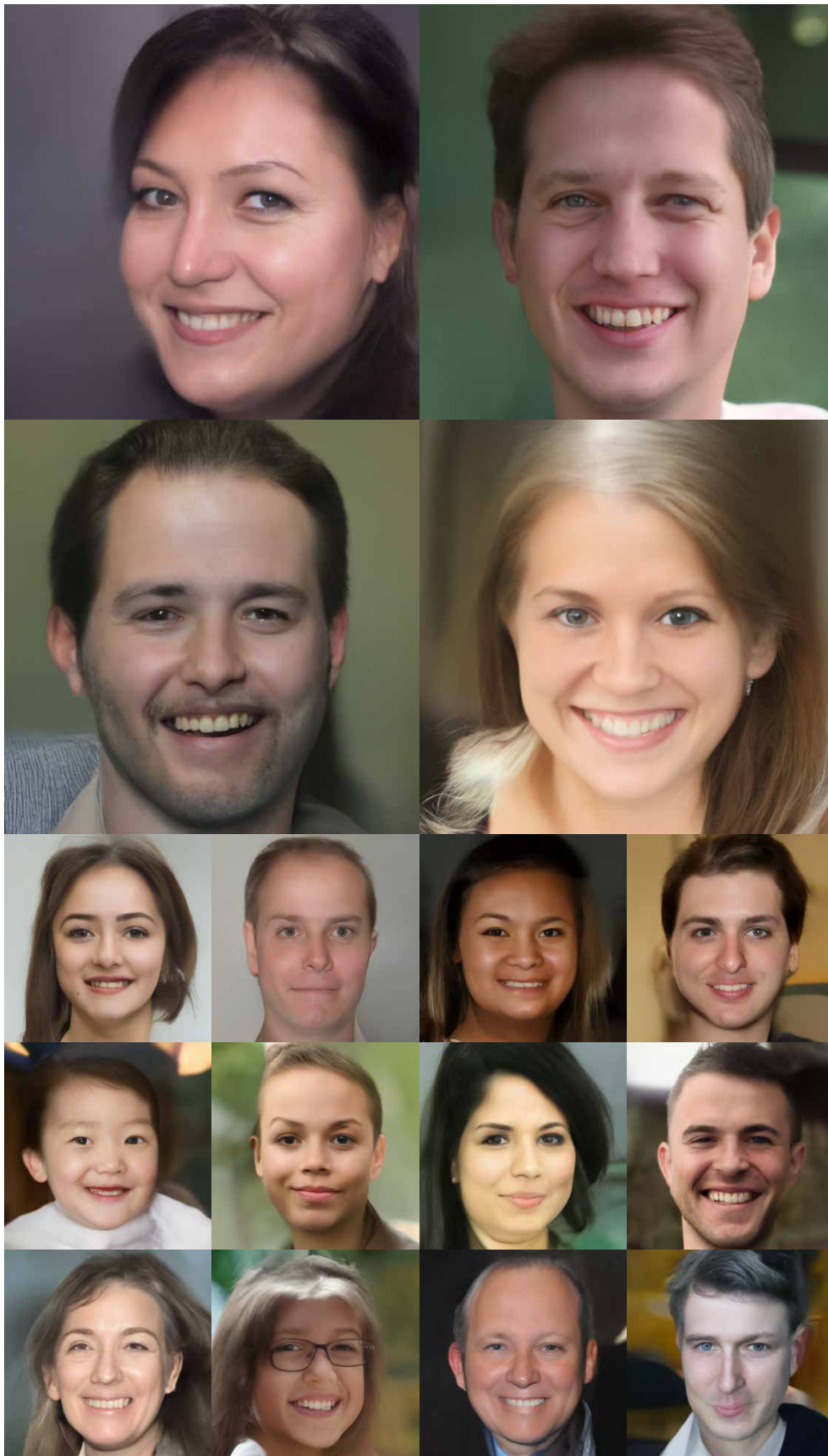


Fig. 10: Facial images at a resolution of 1024×1024 generated by NCSN++ [4] with our PDS. Sampling iterations: 66. Dataset: FFHQ [21].

APPENDIX

EFFECT OF PDS FOR ALLEVIATING ILL-CONDITIONING

We empirically investigate the effect of PDS to reduce the ill-conditioning of the original generation process of SGM. To measure the degree of ill-conditioning, we define the following two metrics: the coordinate variation and V_{coo} (variance across coordinates) and coordinate range R_{coo} (max coordinate value - min coordinate value). For the sample vector $\mathbf{x} \in \mathbb{R}^d$, the coordinate variation V_{coo} is defined as

$$\sum_{i=1}^d (\mathbf{x}_i - \frac{1}{d} \sum_{j=1}^d \mathbf{x}_j)^2,$$

and the coordinate range R_{coo} is defined as

$$\max_i \mathbf{x}_i - \min_i \mathbf{x}_i.$$

Both metrics indicate the gap of the scales in different coordinates, i.e., the degree of the ill-condition issue, with larger R_{coo} and V_{coo} indicate more severe ill-condition issue. We add new experiments, in which we generate some samples through NCSN++ with and without PDS on CIFAR-10, CelebA 64x64 and ImageNet and evaluate the above two metrics. Both metrics are average over all samples and iteration time points for each dataset. As shown in Fig. 11, PDS can reduce both coordinate variation and V_{coo} coordinate range R_{coo} , hence alleviates the ill-condition issue.

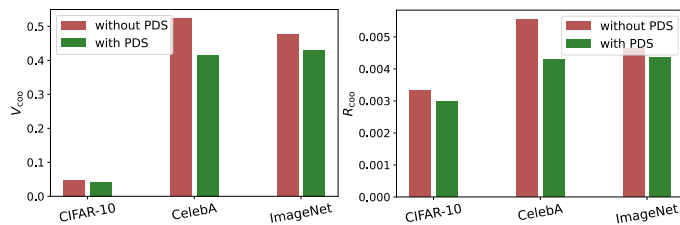


Fig. 11: The coordinate variation V_{coo} and coordinate range R_{coo} of NCSN++ [4] with PDS and without PDS for CIFAR-10, ImageNet and CelebA datasets. We set iterations $T = 100$.

DETAILS OF IMPLEMENTATION

For CIFAR-10, LSUN (bedroom and church, 256×256), and FFHQ (1024×1024), we apply the checkpoints of NCSN++ provided in [4]. We train NCSN++ on CelebA (64×64) for 600k iterations at the batch size of 64 on two NVIDIA RTX 3090 GPUs. We apply the same hyper-parameters of optimizer and learning schedule as [4]. For sampling, we use the same generation process of continuous variance exploding (VE)-NCSN++ [4] with both predictor and corrector, and all the experiments apply the linear schedule used in [4] with both predictor and corrector (PC).

EXTREME LOW ITERATION GENERATION

We investigate the performance of PDS under an extreme low iteration number. We find that the FID score of PDS is 304.71 for generating CIFAR-10 with 20 iterations. While

this performance falls short of state-of-the-art VP SGMs such as DDIM, Analytic-DPM, and PNDM, it still surpasses the baseline NCSN++ model, which yields an FID score of 460.51. This suggests that our PDS still exerts a beneficial influence on the generation process, although it is unable to completely mitigate the issue of ill-conditioning at such low iteration numbers.

One plausible explanation for this phenomenon is the inferior numerical stability of VE SGMs, which includes both the vanilla NCSN++ and our PDS, compared to VP SGMs. Consequently, the PDS faces greater challenges when generating data with a limited number of iterations. Nevertheless, it is essential to highlight that both vanilla NCSN++ and our PDS can achieve superior performance at moderate or higher iteration number, compared to these VP SGMs. As shown in Tab. 2-4 in the main paper, our PDS achieves the best FID across a wide range of iterations, spanning from 100 to 1000. Consequently, our PDS presents a compelling improvement in the balance between generation quality and speed when compared to existing methods.

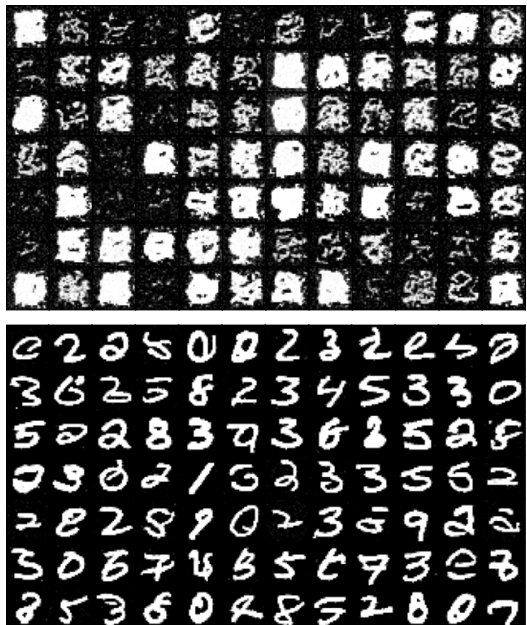


Fig. 12: Sampling using NCSN [2] on MNIST. **Top**: Results by the original sampling method. **Bottom**: Results by our PDS $((r, \lambda) = (0.2H, 1.6))$. Iterations: $T = 20$.

MORE SAMPLES

We provide more samples generated by NCSN++ with PDS in Fig. 16-17.



Fig. 13: Sampling using NCSNv2 [3] on LSUN church (96×96). **Left:** Results by the original sampling method with different sampling iterations. **Right:** Results by our PDS $((r, \lambda) = (0.2H, 1.1))$ with different iterations T .



Fig. 14: Sampling using NCSNv2 [3] on LSUN tower (128×128). **Left:** Results by the original sampling method with different sampling iterations. **Right:** Results by our PDS $((r, \lambda) = (0.2H, 1.6))$ with different iterations T .

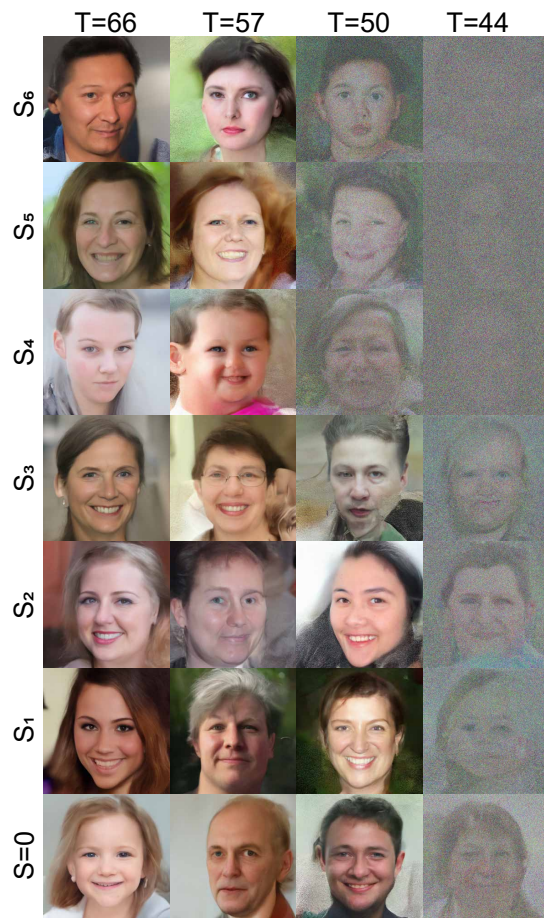


Fig. 15: Facial images generated by NCSN++ [4] with our PDS under different iterations T and different solenoidal items described in Eq. (53)-(57). Dataset: FFHQ [21] (1024×1024).



Fig. 16: CIFAR-10 samples generated by NCSN++ [4] with PDS under different iterations T .

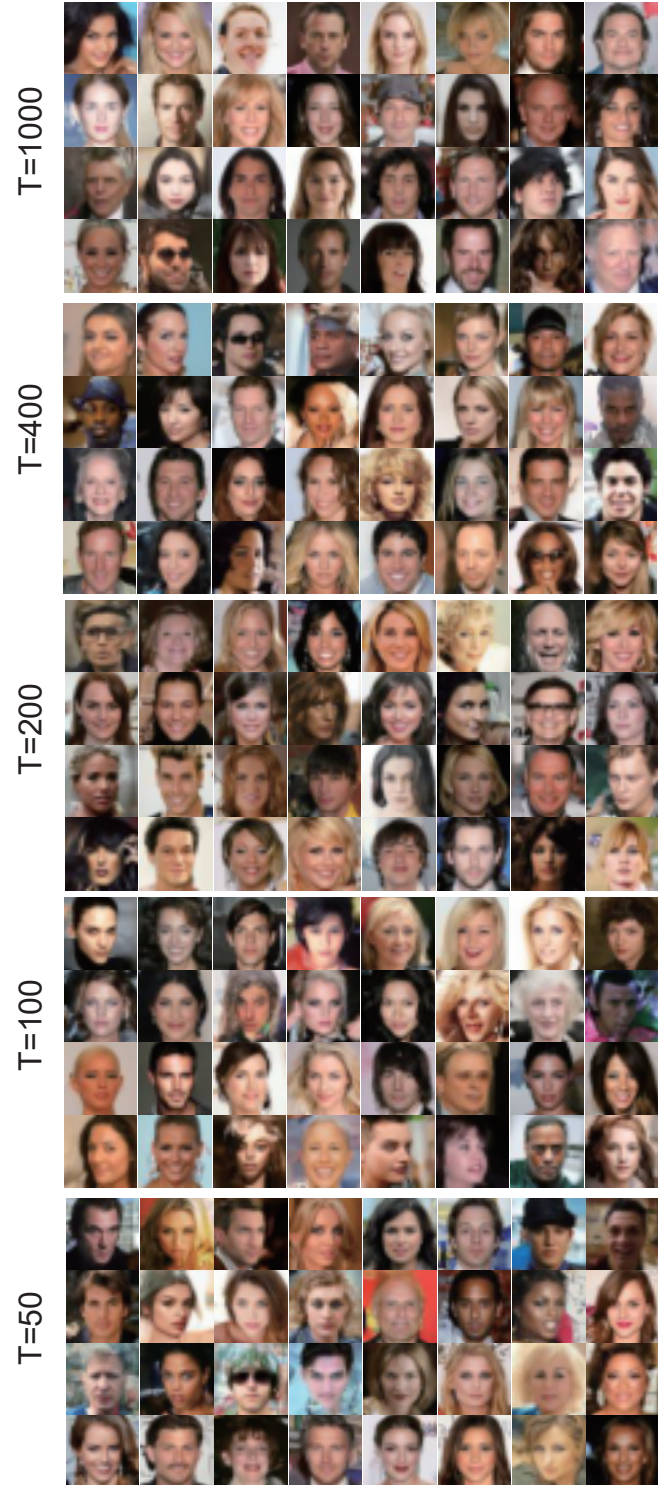


Fig. 17: CelebA (64×64) samples generated by NCSN++ [4] with PDS under different iterations T .

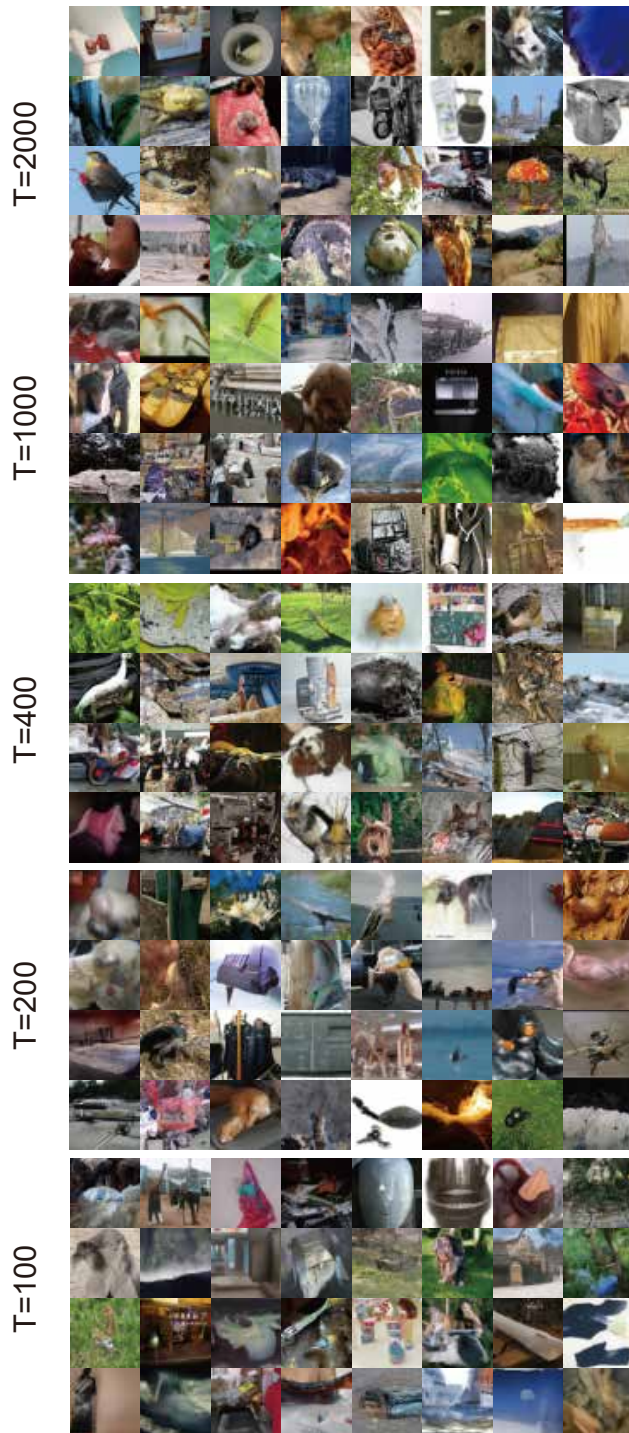


Fig. 18: ImageNet (64×64) samples generated by NCSN++ [4] with PDS under different iterations T .



Fig. 19: COCO (64×64) samples generated by NCSN++ [4] with PDS under different iterations T .



Fig. 20: Sampling using NCSN++ [4] with PDS on LSUN (church and bedroom) at a resolution of 256×256 under iteration numbers 80.

REFERENCES

- [1] I. Goodfellow, J. Pouget-Abadie, M. Mirza, B. Xu, D. Warde-Farley, S. Ozair, A. Courville, and Y. Bengio, "Generative adversarial nets," in *Advances in Neural Information Processing Systems*, 2014. **1, 4**
- [2] Y. Song and S. Ermon, "Generative modeling by estimating gradients of the data distribution," in *Advances in Neural Information Processing Systems*, 2019. **1, 3, 4, 11, 14**
- [3] —, "Improved techniques for training score-based generative models," in *Advances in Neural Information Processing Systems*, 2020. **1, 3, 4, 11, 15**
- [4] Y. Song, J. Sohl-Dickstein, D. P. Kingma, A. Kumar, S. Ermon, and B. Poole, "Score-based generative modeling through stochastic differential equations," in *International Conference on Learning Representations*, 2021. **1, 2, 3, 4, 5, 8, 9, 10, 11, 12, 13, 14, 15, 16, 17, 18**
- [5] Y. Song, C. Durkan, I. Murray, and S. Ermon, "Maximum likelihood training of score-based diffusion models," in *Advances in Neural Information Processing Systems*, 2021. **1**
- [6] Z. Xiao, K. Kreis, and A. Vahdat, "Tackling the generative learning trilemma with denoising diffusion gans," in *International Conference on Learning Representations*, 2022. **1**
- [7] V. De Bortoli, J. Thornton, J. Heng, and A. Doucet, "Diffusion schrödinger bridge with applications to score-based generative modeling," in *Advances in Neural Information Processing Systems*, 2021. **1, 3**
- [8] L. Yang, Z. Huang, Y. Song, S. Hong, G. Li, W. Zhang, B. Cui, B. Ghanem, and M.-H. Yang, "Diffusion-based scene graph to image generation with masked contrastive pre-training," *arXiv preprint arXiv:2211.11138*, 2022. **1**
- [9] Z. Kong, W. Ping, J. Huang, K. Zhao, and B. Catanzaro, "Diffwave: A versatile diffusion model for audio synthesis," in *International Conference on Learning Representations*, 2021. **1**
- [10] N. Chen, Y. Zhang, H. Zen, R. J. Weiss, M. Norouzi, and W. Chan, "Wavegrad: Estimating gradients for waveform generation," in *International Conference on Learning Representations*, 2021. **1**
- [11] A. Nichol, P. Dhariwal, A. Ramesh, P. Shyam, P. Mishkin, B. McGrew, I. Sutskever, and M. Chen, "Glide: Towards photorealistic image generation and editing with text-guided diffusion models," *arXiv preprint*, 2021. **1, 3**
- [12] C. Saharia, W. Chan, S. Saxena, L. Li, J. Whang, E. Denton, S. K. S. Ghasemipour, B. K. Ayan, S. S. Mahdavi, R. G. Lopes *et al.*, "Photorealistic text-to-image diffusion models with deep language understanding," *arXiv preprint*, 2022. **1**
- [13] R. Rombach, A. Blattmann, D. Lorenz, P. Esser, and B. Ommer, "High-resolution image synthesis with latent diffusion models," in *IEEE Conference on Computer Vision and Pattern Recognition*, 2022. **1**
- [14] C. Meng, Y. He, Y. Song, J. Song, J. Wu, J.-Y. Zhu, and S. Ermon, "Sdedit: Guided image synthesis and editing with stochastic differential equations," in *International Conference on Learning Representations*, 2021. **1**
- [15] C. Saharia, W. Chan, H. Chang, C. A. Lee, J. Ho, T. Salimans, D. J. Fleet, and M. Norouzi, "Palette: Image-to-image diffusion models," *arXiv preprint*, 2021. **1**
- [16] C. Saharia, J. Ho, W. Chan, T. Salimans, D. J. Fleet, and M. Norouzi, "Image super-resolution via iterative refinement," *arXiv preprint*, 2021. **1**
- [17] B. Kawar, M. Elad, S. Ermon, and J. Song, "Denoising diffusion restoration models," *arXiv preprint*, 2022. **1**
- [18] J. Ho, T. Salimans, A. Gritsenko, W. Chan, M. Norouzi, and D. J. Fleet, "Video diffusion models," *arXiv preprint arXiv:2204.03458*, 2022. **1**
- [19] L. Zhou, Y. Du, and J. Wu, "3d shape generation and completion through point-voxel diffusion," in *Proceedings of the IEEE/CVF International Conference on Computer Vision*, 2021, pp. 5826–5835. **1**
- [20] A. Brock, J. Donahue, and K. Simonyan, "Large scale GAN training for high fidelity natural image synthesis," in *International Conference on Learning Representations*, 2019. **1**
- [21] T. Karras, S. Laine, and T. Aila, "A style-based generator architecture for generative adversarial networks," in *IEEE Conference on Computer Vision and Pattern Recognition*, 2019. **1, 2, 8, 9, 12, 13, 15**
- [22] T. Karras, T. Aila, S. Laine, and J. Lehtinen, "Progressive growing of gans for improved quality, stability, and variation," in *International Conference on Learning Representations*, 2018. **1**
- [23] G. O. Roberts and O. Stramer, "Langevin diffusions and metropolis-hastings algorithms," *Methodology and computing in applied probability*, 2002. **1, 2, 5**
- [24] M. Welling and Y. W. Teh, "Bayesian learning via stochastic gradient langevin dynamics," in *International Conference on Machine Learning*, 2011. **1, 5, 7**
- [25] M. Girolami and B. Calderhead, "Riemann manifold langevin and hamiltonian monte carlo methods," *Journal of the Royal Statistical Society: Series B (Statistical Methodology)*, 2011. **1, 4, 5**
- [26] C. Li, C. Chen, D. Carlson, and L. Carin, "Preconditioned stochastic gradient langevin dynamics for deep neural networks," in *AAAI Conference on Artificial Intelligence*, 2016. **2, 5**
- [27] C. W. Gardiner *et al.*, *Handbook of stochastic methods*, 1985. **2, 5, 6**
- [28] E. O. Brigham, *The fast Fourier transform and its applications*, 1988. **2, 7**
- [29] T. Dockhorn, A. Vahdat, and K. Kreis, "Score-based generative modeling with critically-damped langevin diffusion," in *International Conference on Learning Representations*, 2022. **3, 10**
- [30] J. Song, C. Meng, and S. Ermon, "Denoising diffusion implicit models," in *International Conference on Learning Representations*, 2020. **3, 9, 10**
- [31] F. Bao, C. Li, J. Zhu, and B. Zhang, "Analytic-dpm: an analytic estimate of the optimal reverse variance in diffusion probabilistic models," *International Conference on Learning Representations*, 2022. **3, 9, 10**
- [32] H. Ma, L. Zhang, X. Zhu, and J. Feng, "Accelerating score-based generative models with preconditioned diffusion sampling," in *European Conference on Computer Vision*, 2022. **3**
- [33] J. Sohl-Dickstein, E. Weiss, N. Maheswaranathan, and S. Ganguli, "Deep unsupervised learning using nonequilibrium thermodynamics," in *International Conference on Machine Learning*, 2015. **3**
- [34] A. Vahdat, K. Kreis, and J. Kautz, "Score-based generative modeling in latent space," in *Advances in Neural Information Processing Systems*, 2021. **3, 10**
- [35] J. Ho, A. Jain, and P. Abbeel, "Denoising diffusion probabilistic models," in *Advances in Neural Information Processing Systems*, 2020. **3, 9, 10**
- [36] P. Dhariwal and A. Nichol, "Diffusion models beat gans on image synthesis," in *Advances in Neural Information Processing Systems*, 2021. **3**
- [37] J. Ho, C. Saharia, W. Chan, D. J. Fleet, M. Norouzi, and T. Salimans, "Cascaded diffusion models for high fidelity image generation," *arXiv preprint*, 2021. **3**
- [38] L. Liu, Y. Ren, Z. Lin, and Z. Zhao, "Pseudo numerical methods for diffusion models on manifolds," in *International Conference on Learning Representations*, 2021. **3, 9, 10**
- [39] D. Kingma, T. Salimans, B. Poole, and J. Ho, "Variational diffusion models," in *Advances in Neural Information Processing Systems*, 2021. **3**
- [40] R. M. Neal *et al.*, "Mcmc using hamiltonian dynamics," *Handbook of markov chain monte carlo*, 2011. **3**
- [41] A. Jolicoeur-Martineau, K. Li, R. Piché-Taillefer, T. Kachman, and I. Mitliagkas, "Gotta go fast when generating data with score-based models," *arXiv preprint arXiv*, 2021. **3**
- [42] T. Salimans and J. Ho, "Progressive distillation for fast sampling of diffusion models," *arXiv preprint arXiv:2202.00512*, 2022. **3**
- [43] C. Meng, R. Rombach, R. Gao, D. Kingma, S. Ermon, J. Ho, and T. Salimans, "On distillation of guided diffusion models," in *Proceedings of the IEEE/CVF Conference on Computer Vision and Pattern Recognition*, 2023, pp. 14297–14306. **3**
- [44] Y. Song, P. Dhariwal, M. Chen, and I. Sutskever, "Consistency models," 2023. **3**
- [45] B. Jing, G. Corso, R. Berlinghieri, and T. Jaakkola, "Subspace diffusion generative models," *arXiv preprint*, 2022. **3, 11, 12**
- [46] A. Q. Nichol and P. Dhariwal, "Improved denoising diffusion probabilistic models," in *International Conference on Machine Learning*, 2021. **3**
- [47] F. Bao, C. Li, J. Sun, J. Zhu, and B. Zhang, "Estimating the optimal covariance with imperfect mean in diffusion probabilistic models," 2022. **3**
- [48] A. Hyvärinen and P. Dayan, "Estimation of non-normalized statistical models by score matching," *Journal of Machine Learning Research*, 2005. **4**
- [49] P. Vincent, "A connection between score matching and denoising autoencoders," *Neural computation*, vol. 23, no. 7, pp. 1661–1674, 2011. **4**

- [50] U. G. Haussmann and E. Pardoux, "Time reversal of diffusions," *The Annals of Probability*, pp. 1188–1205, 1986. 4, 6
- [51] J. Nocedal and S. J. Wright, *Numerical optimization*. Springer, 1999. 5
- [52] H. Risken and J. Eberly, *The fokker-planck equation, methods of solution and applications*, 1996. 5
- [53] S. Wright, J. Nocedal *et al.*, "Numerical optimization," *Springer Science*, vol. 35, no. 67-68, p. 7, 1999. 6
- [54] A. van der Schaaf and J. H. van Hateren, "Modelling the power spectra of natural images: Statistics and information," *Vision Research*, 1996. 6, 11
- [55] K. Friston, "The free-energy principle: a unified brain theory?" *Nature reviews neuroscience*, vol. 11, no. 2, pp. 127–138, 2010. 7
- [56] C.-R. Hwang, S.-Y. Hwang-Ma, and S.-J. Sheu, "Accelerating diffusions," *The Annals of Applied Probability*, 2005. 8
- [57] M. Ottobre, "Markov chain monte carlo and irreversibility," *Reports on Mathematical Physics*, 2016. 8
- [58] L. Rey-Bellet and K. Spiliopoulos, "Irreversible langevin samplers and variance reduction: a large deviations approach," *Nonlinearity*, 2015. 8
- [59] T. Lelièvre, F. Nier, and G. A. Pavliotis, "Optimal non-reversible linear drift for the convergence to equilibrium of a diffusion," *Journal of Statistical Physics*, 2013. 8
- [60] A. Krizhevsky, G. Hinton *et al.*, "Learning multiple layers of features from tiny images," 2009. 8
- [61] Z. Liu, P. Luo, X. Wang, and X. Tang, "Deep learning face attributes in the wild," in *IEEE International Conference on Computer Vision*, 2015. 8
- [62] F. Yu, A. Seff, Y. Zhang, S. Song, T. Funkhouser, and J. Xiao, "Lsun: Construction of a large-scale image dataset using deep learning with humans in the loop," *arXiv preprint*, 2015. 8, 9
- [63] M. Heusel, H. Ramsauer, T. Unterthiner, B. Nessler, and S. Hochreiter, "Gans trained by a two time-scale update rule converge to a local nash equilibrium," in *Advances in Neural Information Processing Systems*, 2017. 8
- [64] A. Brock, J. Donahue, and K. Simonyan, "Large scale gan training for high fidelity natural image synthesis," in *International Conference on Learning Representations*, 2018. 10
- [65] M. Kang, W. Shim, M. Cho, and J. Park, "Rebooting acgan: Auxiliary classifier gans with stable training," *Advances in Neural Information Processing Systems*, vol. 34, pp. 23 505–23 518, 2021. 10
- [66] D. Kim, B. Na, S. J. Kwon, D. Lee, W. Kang, and I.-C. Moon, "Maximum likelihood training of implicit nonlinear diffusion models," *arXiv preprint*, 2022. 10
- [67] J. Deng, W. Dong, R. Socher, L.-J. Li, K. Li, and L. Fei-Fei, "Imagenet: A large-scale hierarchical image database," in *2009 IEEE conference on computer vision and pattern recognition*. Ieee, 2009, pp. 248–255. 9
- [68] T.-Y. Lin, M. Maire, S. Belongie, J. Hays, P. Perona, D. Ramanan, P. Dollár, and C. L. Zitnick, "Microsoft coco: Common objects in context," in *Computer Vision–ECCV 2014: 13th European Conference, Zurich, Switzerland, September 6-12, 2014, Proceedings, Part V 13*. Springer, 2014, pp. 740–755. 9